SLAC-262
UC-34D
(T/E)

QUARK FLAVOR IDENTIFICATION IN ELECTRON-POSITRON ANNIHILATION*

H. Stephen Kaye

Stanford Linear Accelerator Center
Stanford University
Stanford, California 94305

September 1983

Prepared for the Department of Energy

under contract number DE-AC03-76SF00515

Printed in the United States of America. Available from the National Technical Information Service, U.S. Department of Commerce, 5285 Port Royal Road, Springfield, Virginia 22161. Price: Printed Copy A07, Microfiche A01.

---

* Ph.D. dissertation.

Acknowledgments

I am most thankful to my thesis advisor, David Ritson, for the tremendous store of good advice that he gave me, most of which I eventually heeded. Without his bursts of enthusiasm tempered with patience and respect for opinions not his own, this thesis might never have been attempted.

Various members of the MAC Collaboration deserve thanks for having designed and constructed the MAC detector, its electronics, and its software, and for collecting and processing the data that enable this analysis to be carried out. Special thanks go to Keith Rich, who designed and managed our superb data flow system, to Bill Ford, for good advice and for providing direction to the collaboration in time of need, and to Kwong Lau and Scott Clearwater, for helpful discussions.

I thank Michael Peskin and Stanley Wojcicki for their helpful comments regarding this thesis. The preparation of this thesis was aided tremendously by the typesetting system TeX, which was written by Donald Knuth of the Stanford Computer Science Department, and made available at SLAC through the efforts of several people, most notably Roger Chaffee, to whom I extend my gratitude.

My thanks to Pat and Gerry Morgan, to Oscar Gaytan, and to Maureen Richards for friendship and encouragement.

This work is dedicated to the memory of my father, to my mother, and to Mitch LaPlante.

Table of Contents

List of Figures

List of Tables

Chapter 1

Introduction

To the great misfortune of the experimental physicist, one of the principal objects of current theoretical speculation is almost entirely hidden from view. Quarks, the proposed principal constituents of all hadrons, are almost universally believed to exist, but they have never been, and possibly will never be, seen in the laboratory. Unlike the leptons, whose presence is unmistakable, they are so well disguised behind the jets of hadrons that they create, that their properties, both under the strong and weak interactions, remain largely unmeasured, especially the properties of the heavier, more recently discovered, quarks.

Yet it is essential both to the verification of the standard model of weak-electromagnetic unification and to the general understanding of the strong interaction that the heavy quarks be studied. Electroweak unification makes definite predictions as to the relative number of quarks and leptons, the weak decays of the quarks, and the angular distribution of their production. And our understanding of the strong interaction is glaringly incomplete as long as we do not know how hadrons are spontaneously created upon the production of quark pairs. With such knowledge, the predictions of the various models of quark dynamics can be tested.

Experimentally, the task of separating events according to the type (or flavor) of their parent quarks is an extremely difficult one. Not only are large numbers of hadrons created, but they are concentrated in a narrow cone around the initial quark axis, so that separate detection of individual hadrons becomes very difficult. Even when they can be separated, their indistinguishability makes reconstruction of their parent particles impossible, except in rare cases.

Fortunately, the weak decays of the quarks provide us with a tool which, as will be demonstrated, can serve as a clue to the identity and properties of the primary particle. Leptons produced in the decays of the heavy quarks can be detected, and can serve as a signature of these events. The momenta and transverse momenta of the leptons themselves provides a considerable amount of useful information as to the mass, charge, decays, and fragmentation of the quarks, and the hadronic jets of the semileptonic events can be studied to obtain additional information.

The analysis described in this volume makes use of muons to signal the presence of heavy quarks. The advantage of muons over electrons is that they are more readily identified, since their easy penetration of steel, as compared to that of hadrons, separates them spatially from the rest of the event. They are therefore less prone to backgrounds from misidentified hadrons.

The MAC detector at PEP, data from which is described herein, is especially well suited to inclusive muon measurements. It provides muon tracking over a large solid angle, good momentum determination of muons, and sufficient material to separate muons from energetic hadrons adequately. Its finely segmented calorimetry and outer drift system provide sufficient redundancy to

eliminate backgrounds in most cases. And the nearly full solid angle coverage of the calorimeters makes certain properties of the jets measurable with greater reliability than detectors that rely either on the detection of only charged particles or on calorimetry in a restricted angular region.

The following chapters describe the theoretical issues relevant to inclusive muon analysis, the MAC detector and its data flow structure, the identification of muons in hadronic events and the measurement of their momenta, and the selection of events so as to minimize background. Experimental results are presented describing the fragmentation of heavy quarks into hadrons, the semimuonic branching fractions of the heavy quarks, the asymmetry in the angular distribution of the heavy quarks, and the invariant mass and charged multiplicity of heavy quark jets. In addition, lower limits are set on the masses of certain proposed particles that are expected to decay semileptonically. Finally, events containing two muons are analyzed in order to investigate the possibility of mixing in the B–$\bar{B}$ system and whether the b might form its own SU(2) singlet.

Chapter 2

Quarks, Hadrons, and Flavor

In electron-positron annihilation at relatively high energy, charged particle-antiparticle pairs are created in a well-understood manner through the electromagnetic interaction.[1] Pairs of leptons can easily be observed, and they follow the predictions of Quantum Electrodynamics (QED) in their overall cross sections and angular distributions. On the other hand, it is rare for pairs of hadrons to be detected unaccompanied by other particles in an event. More typically, ten to twenty hadrons are produced, often in two (or more) collimated "jets" of particles suggesting that they originate from pairs of primary particles. The total cross section for the production of these events is large—approximately four times that for muon pairs—which suggests that several varieties of parent particles exist.

2.1 Quantum Chromodynamics

The theory of strong interactions that has best explained the cross section and jet properties of hadronic events, as well as the phenomenology of interactions of various hadrons, is Quantum Chromodynamics (QCD). QCD holds that the hadrons that we observe are composite particles made up of two or three particles called "quarks." A meson is composed of a quark and an antiquark, while a

---

[1]Neglecting, for a few pages, the effect of the weak interaction.

baryon is made up of three quarks. Quarks were introduced, in an attempt to create a "periodic table" for the hadrons, by Gell-Mann[2] and by Zweig[3] in 1964. They are spin-$\frac{1}{2}$ fermions that have either $-\frac{1}{3}$ or $+\frac{2}{3}$ unit of electric charge, depending on the type, or "flavor," of quark. Three flavors of quarks were originally proposed.

As the predicted cross section for the creation of particle-antiparticle pairs is proportional to the square of the charge of the particle, the large observed rate of production of hadronic events, as compared to muon pairs, could hardly be explained by the presence of two quarks with $-\frac{1}{3}$ charge and one with charge $+\frac{2}{3}$, which would result in

$$R = \frac{\sigma_{hadrons}}{\sigma_{\mu^+\mu^-}} \approx \sum_{flavors} q^2_{quark} = \frac{2}{3}.$$

In order to explain the preference for $q\bar{q}$ and qqq states, Han and Nambu[4] , first postulated, in 1965, an internal quantum number for the quarks. Such a quantum number is now called "color."[5] Each quark can have one of three colors, which trivially allows the presence of the three-quark state, as each quark can have different quantum numbers. Ordinary hadrons are then color singlets, meaning that they themselves have no color. This additional property triples the expected cross section,[6] as the sum in the R-equation must now be taken over colors as well as flavors.

---

[2]M. Gell-Mann, Phys. Lett. **8**, 214 (1964).
[3]G. Zweig, CERN Report no. TH 401:412 (1964).
[4]M. Y. Han and Y. Nambu, Phys. Rev. **B139**, 1006 (1965).
[5]O. W. Greenberg, Phys. Rev. Lett. **13**, 598 (1964).
[6]J. D. Bjorken, Phys. Rev. **179**, 1547 (1969).

Further evidence for the composite nature of hadrons comes from the limited transverse momenta observed in hadron-hadron collisions, which prompted Feynman[7] to propose, in 1969, that hadrons had constituents, which he called "partons." Quantum Chromodynamics then began to develop, under the leadership of several authors[8] as a non-abelian gauge theory of the strong interaction, based upon the simple concepts of "quarks" and "color."

A Lagrangian has been constructed for QCD that, like the one for QED, describes the interactions of spin-$\frac{1}{2}$ fermions (the quarks) and vector bosons (called "gluons") that mediate the interaction. QCD differs from QED principally in that gluons, unlike the photons of QED, are themselves carriers of the charge of the interaction (color). And unlike QED, this charge appears to manifest itself only within hadrons, never revealing itself in any long-range interaction.

While QED can be successfully solved using perturbative methods, the coupling constant for the strong interaction (α_s) is much larger than that for electromagnetism (α), and therefore the perturbative method is useful only for limited applications of QCD. Basically, only properties in which the partons[9] are important individually, rather than collectively as hadrons, can be studied perturbatively. This means, unfortunately, that the masses of the hadrons are not

---

[7]R. P. Feynman, Phys. Rev. Lett. **23**, 1415 (1969) and *Photon-Hadron Interactions*, (Benjamin, New York, 1972).

[8]D. J. Gross and F. Wilczek, Phys. Rev. Lett. **30**, 1343 (1973) and Phys. Rev. **D8**, 3633 (1973);
H. D. Politzer, Phys. Rev. Lett. **30**, 1346 (1973);
H. Fritzsch, M. Gell-Mann, and H. Leutweyler, Phys. Lett. **B47**, 365, (1973);
S. Weinberg, Phys. Rev. Lett. **31**, 494 (1973);
G. t'Hooft, Nucl. Phys. **B33**, 73 (1973).

[9]Henceforth, "parton" is used to mean a quark, an antiquark, or a gluon.

predicted, nor is the manner in which hadrons are formed by the combining of partons. But production cross sections and angular distributions of jets are predicted, as are the radiative corrections that produce 3– and 4–jet events through $q\bar{q}g$ and $q\bar{q}gg$ states.

2.2 Quark Flavors

The original quark model contains three flavors of quarks, named *up*, *down*, and *strange*. The d and s quarks have a charge of $-\frac{1}{3}$ times the positron charge, while the u quark has $+\frac{2}{3}$ charge. The proton contains two u quarks and one d quark, while the neutron has two d's and one u. Charged and neutral pions are made up of appropriate combinations of these two quarks as well. Kaons and Λ particles contain one s quark, and so on. All of the hadrons known in mid-1974 could be explained as being composed of the three quark flavors in some combination. The flavors are conserved by the strong interaction but not the weak.

In 1970, Glashow, Iliopoulos, and Maiani[10] (GIM) proposed the existence of an additional heavier quark, with flavor they called *charm*, as part of an explanation of the suppression of neutral strangeness-changing decays. In the "standard" weak-electromagnetic unification model of Weinberg,[11] Salam,[12] and Glashow,[13] the GIM mechanism successfully explains the suppression of such decays for a charmed quark mass between 1 and 2 GeV. The discovery, in

---

[10]S. L. Glashow, J. Iliopoulos, and L. Maiani, Phys. Rev. **D2**, 1285 (1970).
[11]S. Weinberg, Phys. Rev. Lett. **19**, 1264 (1967).
[12]A. Salam, *Elementary Particle Physics: Relativistic Groups and Analyticity*, edited by N. Svartholm, (Almquist & Wiksell, Stockholm, 1968), p. 367.
[13]S. L. Glashow, Nucl. Phys. **22**, 579 (1961).

late 1974, of a very narrow resonance in hadron production at 3.1 GeV[14] required the presence of such a new flavor and also provided striking evidence for the quark model. Because the resonance was so narrow, the particle produced (called ψ or J) must have had constituents that were unable to decay via the strong or electromagnetic interactions. They therefore had to possess some quantum number that could be violated only weakly, such as charm. The discovery of other resonances at somewhat higher energies led to the classification of the various particles as excited states of a $c\bar{c}$ pair—charmonium, in close analogy with the e^+e^- "atom" positronium.

Since

$$R = \frac{\sigma_{hadrons}}{\sigma_{\mu^+\mu^-}} \approx \sum_{colors} \sum_{flavors} q^2_{quark},$$

it is expected that the production of a new quark flavor would result in a change in R. The c quark is found to have a charge of $+\frac{2}{3}$, so the expected change in R is $3(\frac{2}{3})^2 = \frac{4}{3}$. Figure 2–1 shows the measured values of R for a variety of center-of-mass energies, and the expected behavior is visible. Below the charm threshold, $R \approx 2$, and a definite increase is apparent above the threshold. The predicted value is actually somewhat higher than that given in the equation above, as it is increased by addition of terms obtained from peturbative QCD. The increase in the cross section just above the charm threshold is due to the presence of resonances of "charmonium" states.

With four quarks (two having each of two different charges) and two sets

---

[14] J. Aubert *et al.*, Phys. Rev. Lett. **33**, 1404 (1974);
J.-E. Augustin *et al.*, Phys. Rev. Lett. **33**, 1406 (1974);
G. S. Abrams *et al.*, Phys. Rev. Lett. **33**, 1453 (1974).

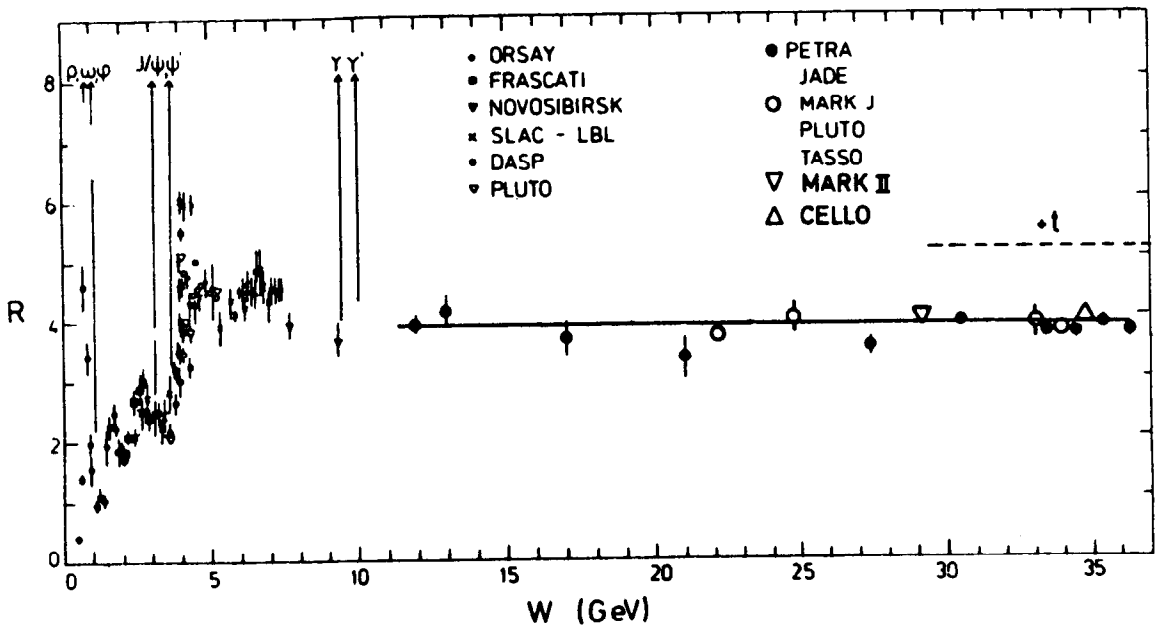

Figure 2–1: Measurements of $R = \frac{\sigma_{hadrons}}{\sigma_{\mu\mu}}$ at various center-of-mass energies.

of leptons (each set having a lepton of unit charge and a neutrino partner), it was attractive to put the lighter (u and d) and heavier (c and s) quarks into "families" in symmetry with the leptons. The standard electroweak model does exactly this, putting pairs of leptons or quarks into left-handed doublets and right-handed singlets. In order that the theory be renormalizable, equal numbers of families of leptons and quarks are required to exist; the so-called triangle anomalies[15] are canceled only in the presence of such a symmetry.[16]

The discovery of the τ lepton[17] in 1975 suggested that yet another family of quarks should exist at higher energies. On schedule, in 1977, a new particle (the Υ), was discovered[18] as an enhancement in the invariant mass spectrum of muon pairs produced in pp collisions, with a mass of 9.5 GeV. The new quark flavor assigned to the constituents of the Υ has been called *bottom* or *beauty*, and has a charge of $-\frac{1}{3}$. As with the c, several other resonances, understood as excited states of the $b\bar{b}$ system, have been found. A $+\frac{2}{3}$ charged partner of the b, referred to as *top* or *truth* has not been discovered, nor has any member of some still higher-energy family that may exist. While the completion of the latest family requires the existence of the t, its mass is not predicted with any certainty. There is no theoretical basis for the existence or non-existence of a fourth family, and there are no estimates for the masses of the members of such

---

[15]S. L. Adler, *Lectures on Elementary Particles and Quantum Field Theory*, edited by S. Deser *et al.*, (MIT, Cambridge, 1970);
D. J. Gross and R. Jackiw, Phys. Rev. **D6**, 477 (1972).

[16]Unless exotic leptons exist in isospin triplets; see H. Georgi, S.L. Glashow, Nucl. Phys. **B159**, 29 (1979).

[17]M. L. Perl *et al.*, Phys. Rev. Lett. **35**, 1489 (1975).

[18]S. W. Herb *et al.*, Phys. Rev. Lett. **39**, 252 (1977).

a family. It is even possible that they might have masses comparable to that of the t quark.

2.3 Weak Decays of Heavy Quarks

From observations of the decay products of mesons containing charm, it is known that the principal decay modes of charmed mesons all involve strange particles. A fraction of these decays also contain a lepton and its neutrino, which, as described in later chapters, provides a signature for charmed events.

The decay products of mesons containing the b quark are less well known. For three families of quarks as described above, a matrix of couplings has been introduced to describe charged current interactions (the Kobayashi-Maskawa matrix[19]) among the quarks. It contains four parameters, of which three are expressed as angles and one as a complex phase. By examining the couplings of the u quark to the d and the s, and the mixing of the K°-$\bar{K}^\circ$ system, limits have been set on the angles describing the relative coupling of the b to the u and the c. These limits suggest that the predominant decay modes of the B mesons contain charmed mesons. This expectation has recently been confirmed by experiment.[20] The cascade $b \rightarrow c \rightarrow s$ is therefore expected to dominate. Semileptonic decays have also been observed for the B (see Chapter 6).

The same constraints on the coupling matrix predict that mesons containing the t will decay to bottom mesons. The cascade $t \rightarrow b \rightarrow c \rightarrow s$ is expected.

---

[19]M. Kobayashi and K. Maskawa, Progr. Theor. Phys. **49**, 652 (1973).
[20]D. Andrews *et al.*, Cornell Report No. CLNS 82/547.

2.4 HADRONIZATION

When a quark-antiquark pair is created in its center of mass at an energy well above threshold, the partons must move apart to conserve energy. But since jets of hadrons are commonly observed instead of single quarks, the quarks must somehow cause the formation of hadrons. Just as electromagnetic fields can draw charged particle-antiparticle pairs from the vacuum, according to QED, the color field surrounding a single quark draws quark-antiquark pairs from the "sea." It can be readily imagined that one member of such a pair combines with one of the single primary partons to form a meson, leaving the other member of the pair to fend for itself. But this leftover quark could draw another pair from the sea, form a meson of its own, leaving another unmatched quark. As the number of hadrons produced is finite, there will always be a leftover quark, whose naked color would violate our understanding of QCD, and whose fractional charge would conflict with experimental observation.

The other primary parton, under such a scheme, would hadronize in the same way, so a pair of lone partons (one quark and one antiquark) remains for each event. In some way or another, it seems, the two hadron jets maintain awareness of each other's existence long enough that there are no unmatched partons remaining following the hadronization. Experimental results indicate that baryons are present in hadronic jets—this can be accounted for if two pairs of partons are simultaneously created, and one quark from each pair combines with the leftover quark from the previous pair.

Because of the lack of a non-perturbative solution to QCD, no solid prediction exists as to the exact method by which jets communicate, to the manner in

which momentum is distributed among the hadrons, or to the number of hadrons produced in a jet. Some models exist that provide answers to these questions, the popular favorite of which is an ansatz proposed by Field and Feynman,[21] which was designed to be convenient for Monte Carlo use. If the interaction $e^+e^- \rightarrow q_1\bar{q}_1$ takes place (the subscripts denote a particular quark of flavor f_1), quark q_1 will cause a pair $q_2\bar{q}_2$ to be created, and q_1 and $\bar{q}_2$ will form meson M_1. The flavor f_2 is determined probabilistically, with the experimentally observed preference for light mesons indicating that light quarks are strongly favored. Another pair, $q_3\bar{q}_3$, is drawn from the sea, and meson M_2 is constructed from $q_2\bar{q}_3$, and so on.

The momentum distribution of mesons M_n is determined in the following way: if

$$z = \frac{(E+p_{||})_{M_n}}{(E+p_{||})_{q_n}},$$

with $p_{||}$ equal to the component of p in the direction of p_{q_1}, then $D_{f_n}(z)$ is defined as the probability distribution for z. In other words, $D_{f_n}(z)$ determines the likelihood of M_n's carrying off any given fraction z of its parent quark's initial $E+p_{||}$. The remaining $E+p_{||}$ is carried off by quark q_{n+1}. The model has been quite successful at reproducing the momentum spectrum of hadrons containing light quarks, with $D(z)$ peaked at z near zero. The transverse momentum of the hadrons is simply given a random value consistent with the observation of limited ($\approx$ 300 MeV) transverse momentum in hadrons.

The fragmentation (i.e., hadron formation) process stops when $(E+p_{||})_{q_n}$ is

---

[21] R. D. Field and R. P. Feynman, Nucl. Phys. **B136**, 1 (1977) and Phys. Rev. **D15**, 2590 (1977).

less than some minimum value, which is adjusted so that the number of hadrons produced agrees with experiment. Antiquark $\bar{q}_1$ goes through the same process. When all is done, the two leftover partons are unceremoniously combined.

Regardless of whether the model is physically appealing, it does serve to predict the momentum spectrum of hadrons in multihadron events, and to allow the simulation of hadronic events. The fragmentation function $D_q(z)$, for quark flavor q, has become a standard subject of study. Since most observed mesons contain only light quarks, the function has been well determined for light flavors. For heavy quarks, the fragmentation function has undergone much less scrutiny.

Using simple kinematic arguments, Bjorken[22] and Suzuki[23] were the first to speculate that the fragmentation function for heavy quarks should be peaked at larger values of z, and should be an increasing function of quark mass. The functional form of $D_q(z)$ is not known. Some formulas that have been suggested are presented in Chapter 6.

In the case of $e^+e^- \rightarrow b\bar{b}$, the b jet can serve as an example of the effect of fragmentation on the products of weak decay. Figure 2–2 shows a b parent quark ($= q_1$) combining with a $\bar{u}$ quark ($= \bar{q}_2$) to form a B^- meson ($= M_1$), and the continuing fragmentation chain described above. In this case, the B meson decays semimuonically ($B^- \rightarrow D^0\mu^-\bar{\nu}_\mu$). The b quark fragmentation function will determine the momentum spectrum of the B mesons, which, in such a decay mode, will determine the boost given to the muon. Figure 2–3 shows the momentum spectrum of muons created in the decay of B mesons

---

[22]J. D. Bjorken, Phys. Rev. **D17**, 171 (1978)
[23]M. Suzuki, Phys. Lett. **71B**, 139 (1977).

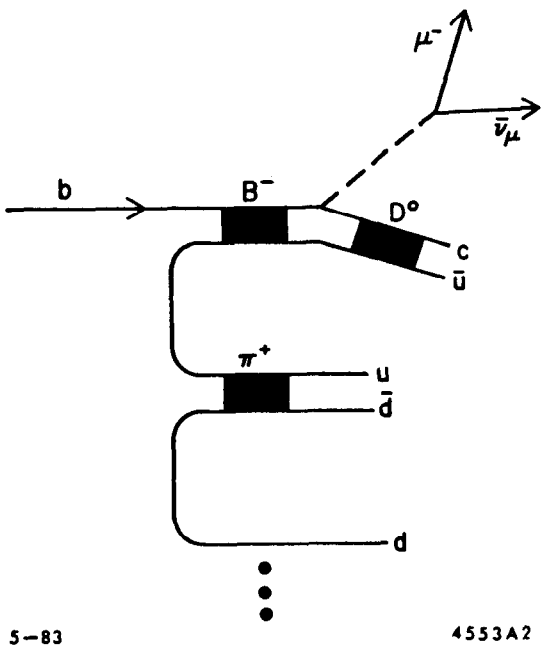

Figure 2–2: The fragmentation of a b quark, and subsequent semileptonic decay of the B meson.

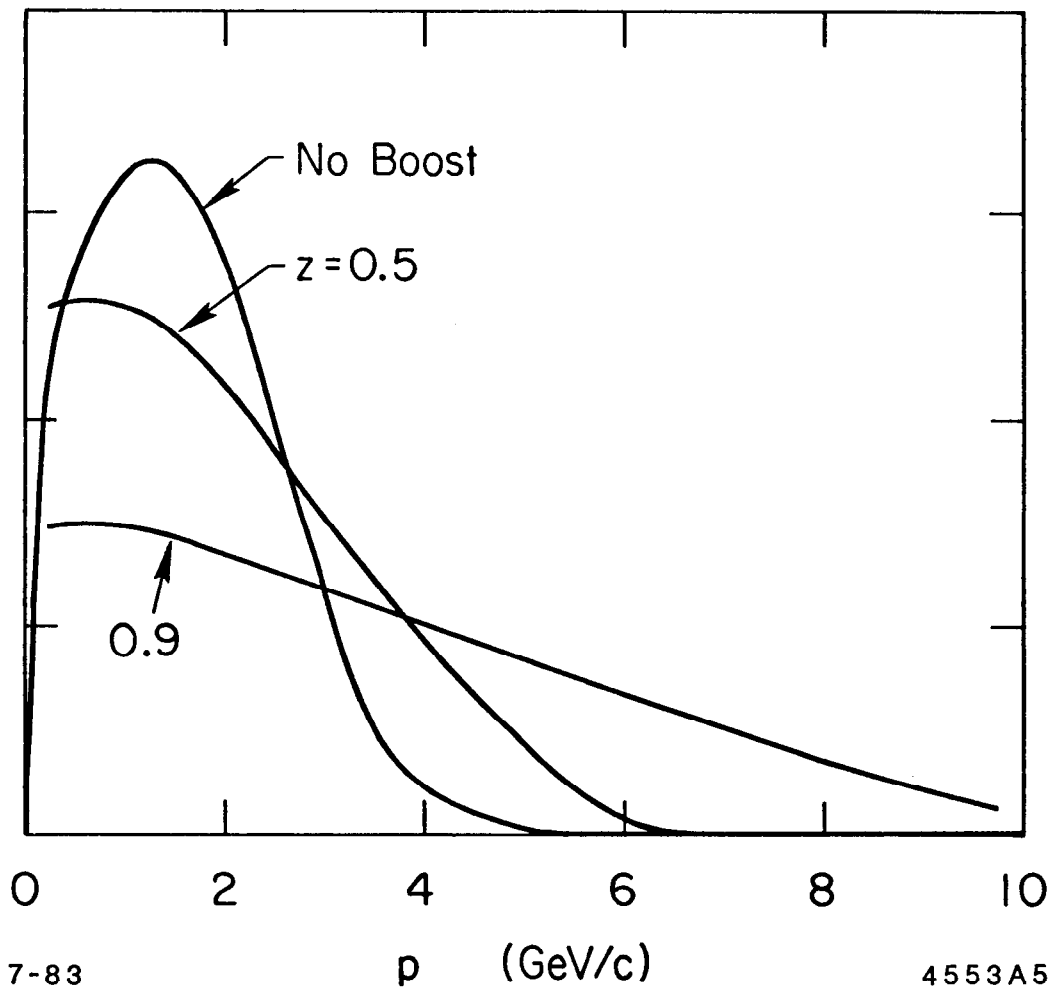

Figure 2–3: The momentum spectrum of muons from B meson decay (no detector effects included) with no boost applied, with $z = .5$, and $z = .9$, for $E_{beam} = 14.5$ GeV.

either at rest, or moving with momentum equivalent to $z = .5$ or $z = .9$, for beam energy of 14.5 GeV. Clearly, the spectrum is highly sensitive to $D_b(z)$.

The component of muon momentum transverse to the B direction is Lorentz invariant to the boost, but if a cut is applied on the total momentum of the muons, the observed spectrum will change drastically in normalization and slightly in shape depending on the magnitude of the boost (see Figure 2–4). But because of its largely invariant shape, the $p_\perp$ spectrum of the muons serves as a fragmentation-independent indicator of the mass of the decaying particle.

2.5 Weak-Electromagnetic Interference

The quark-antiquark pair is ordinarily produced via a virtual photon, in the reaction $e^+e^- \rightarrow \gamma \rightarrow q\bar{q}$. But the standard unification of the weak and electromagnetic interactions postulates the existence of intermediate vector bosons, with masses in the vicinity of 80–100 GeV, of which one, the Z°, is neutral and can take the place of the virtual photon: $e^+e^- \rightarrow Z^\circ \rightarrow q\bar{q}$.

The addition of this process changes the total cross section slightly, at the energy of this analysis. A more dramatic change is made in the angular distribution of events: an asymmetry is introduced in the distribution of quarks *versus* antiquarks. The differential cross section for the creation of a fermion-antifermion pair is given by[24]

$$\frac{d\sigma(e^+e^- \rightarrow f\bar{f})}{d\cos\theta} = \frac{\pi\alpha^2}{2s}\Big(Q_f^2(1+\cos^2\theta) - 2Q_f\chi[g_V^e g_V^f(1+\cos^2\theta) + 2g_A^e g_A^f \cos\theta] + O(\chi^2)\Big),$$

---

[24] J. Ellis, LAPP Report no. LAPP-TH-48 (1981).

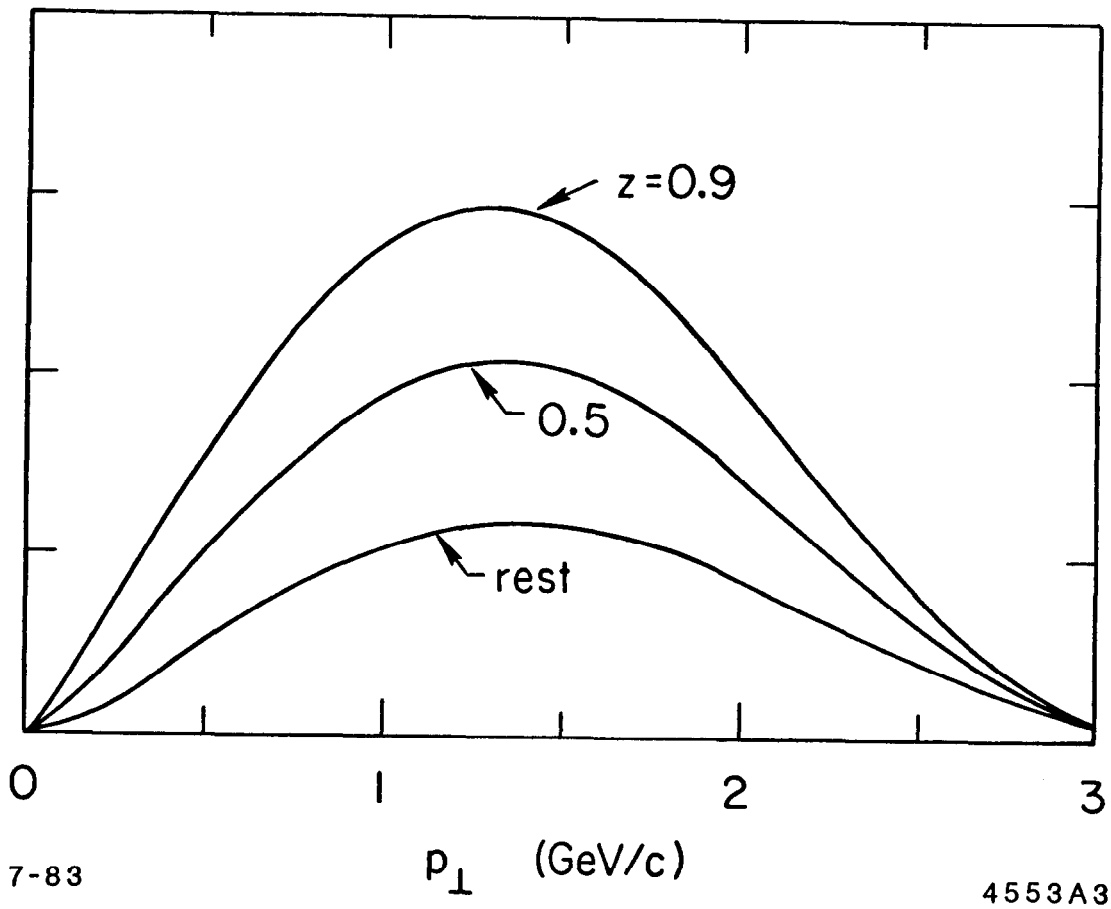

Figure 2–4: Transverse momentum spectrum of muons with $p > 2$ GeV/c from B decay, for B's at rest and with $z = .5$ and .9 ($E_{beam} =$ 14.5 GeV.)

where g_V and g_A are the vector and axial vector couplings of the specified particles in the model,

$$\chi = \left(\frac{G_F}{2\sqrt{2}\pi\alpha}\right)\frac{m_Z^2 s}{s - m_Z^2} \approx .164$$

for $m_Z = 94$ GeV and $\sqrt{s} = 29$ GeV, and, importantly, *θ is the angle between the fermion and the incident electron direction.* The first term in the cross section is the pure electromagnetic contribution (without radiative correction).

The predicted values for g_A and g_V are shown below for the various fermions:

Particles	g_A	g_V
e, μ, τ	$-\frac{1}{2}$	$-\frac{1}{2} + 2\sin^2\theta_W \approx 0$
u, c, t	$+\frac{1}{2}$	$+\frac{1}{2} - \frac{4}{3}\sin^2\theta_W \approx \frac{1}{6}$
d, s, b	$-\frac{1}{2}$	$-\frac{1}{2} + \frac{2}{3}\sin^2\theta_W \approx -\frac{1}{3}$

in which the experimentally determined value of $\sin^2\theta_W \approx \frac{1}{4}$ has been used to estimate g_V. Various experiments[25] have tended to confirm the values of g_A for electrons, muons,[26] and of up and down quarks, and of g_V for electrons and up and down quarks.

If these values are accepted, the term in $g_V^e g_V^f$ will be small, so the fractional change in the differential cross section due to the neutral current is

$$\frac{\left(\frac{d\sigma}{d\cos\theta}\right)^{Electroweak}}{\left(\frac{d\sigma}{d\cos\theta}\right)^{QED}} = -\frac{4\chi}{Q_f} g_A^e g_A^f \frac{\cos\theta}{1 + \cos^2\theta}.$$

---

[25] J. E. Kim, P. Longacker, M. Levine, and H. H. Williams, Rev. Mod. Phys. **53**, 211 (1981).

[26] E. Fernandez *et al.*, Phys. Rev. Lett. **50**, 1238 (1983).

Because of its $\frac{1}{Q_f}$ dependence, the effect is three times more pronounced for $b\bar{b}$ production than for muon pairs.

The deviation in the predicted angular distribution is plotted in Figure 2–5 for the various fermions. It is instructive (if not very useful experimentally) to integrate the above expression over the full solid angle separately for $\theta < 90°$ and $\theta > 90°$, and two take the difference between the two hemispheres as the overall forward-backward asymmetry. It is found that $\frac{\sigma(\theta<90°)-\sigma(\theta>90°)}{\sigma_{total}}$ is -6.1% for $\mu^+\mu^-$ or $\tau^+\tau^-$, -9.2% for $u\bar{u}$ and $c\bar{c}$, and -18.5% for $d\bar{d}$, $s\bar{s}$, and $b\bar{b}$ production.

The leptons, which have the smallest asymmetry, allow easy charge measurement. Hadronic jets, on the other hand, mask both the charge and the flavor of the parent quarks. Even when the charge is measureable, such as via identification of the products of the weak decays of the primary mesons, the flavor still must be determined in order to test weak-electromagnetic unification. Since the asymmetry is predicted to be negative for all fermions, positively charged fermions (u, c) will be produced in excess in the same hemisphere as negatively charged fermions (d, s, b) are in excess. The asymmetry is therefore partly canceled out if the flavor is not determined.

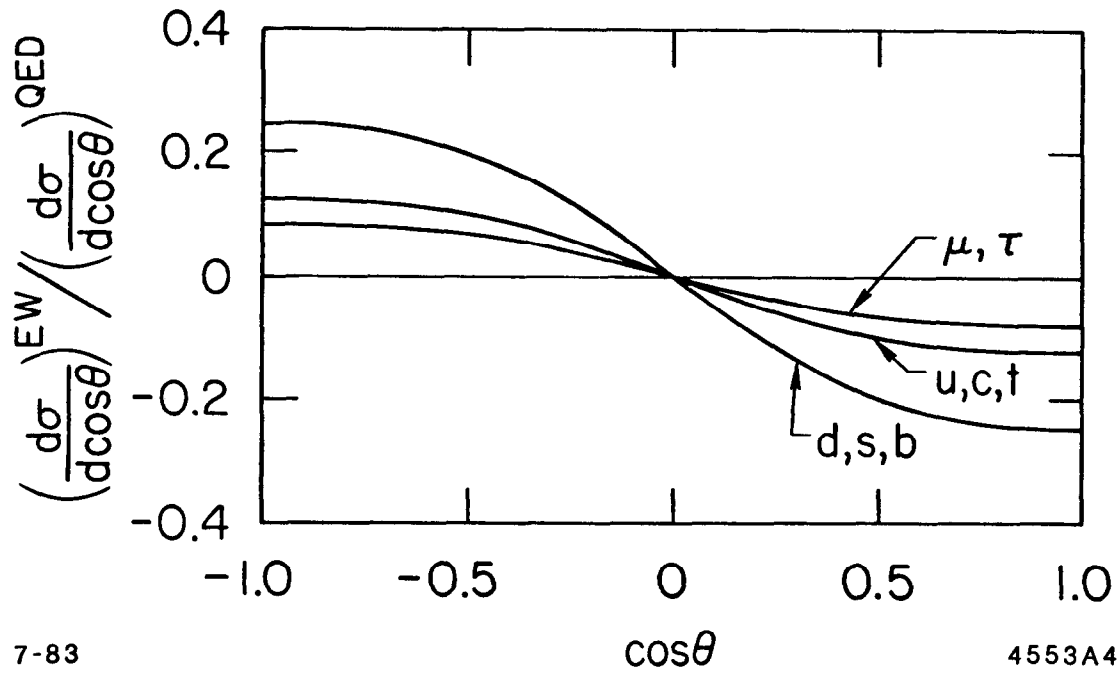

Figure 2–5: Fractional change in the differential cross section for fermion pair production due to weak-electromagnetic interference.

Chapter 3

The MAC Detector

The MAC (for "Magnetic Calorimeter") Detector was designed to be a general purpose detector for final states in electron-positron annihilation, with emphases placed on the obtaining of calorimetric information for as close to total solid angle as possible and on the identification of leptons. The detector was assembled, from parts made at the various collaborating institutions, in Interaction Region 4 of the PEP storage ring at SLAC, beginning in the summer of 1979. First data were taken in the autumn of 1980, and the acquisition of data continues at the time of this writing. Drawings of the detector appear in Figures 3–1 and 3–2.

Throughout the following description, the z-axis is defined to be along the beam path, with positrons travelling in the positive z-direction. The polar angle θ is defined from the positive z-axis. The origin of coordinates is chosen to be the point at which the centers of the positron and electron bunches meet.

3.1 Inner Drift Chamber

The vacuum chamber containing the beam path has a radius of 4.1 cm and is encased in an aluminum pipe with a thickness of 1.8 mm. A cylindrical drift chamber surrounds the beam pipe to provide tracking of charged particles. It consists of 833 cells arranged in ten layers, with the innermost layer at a radius of

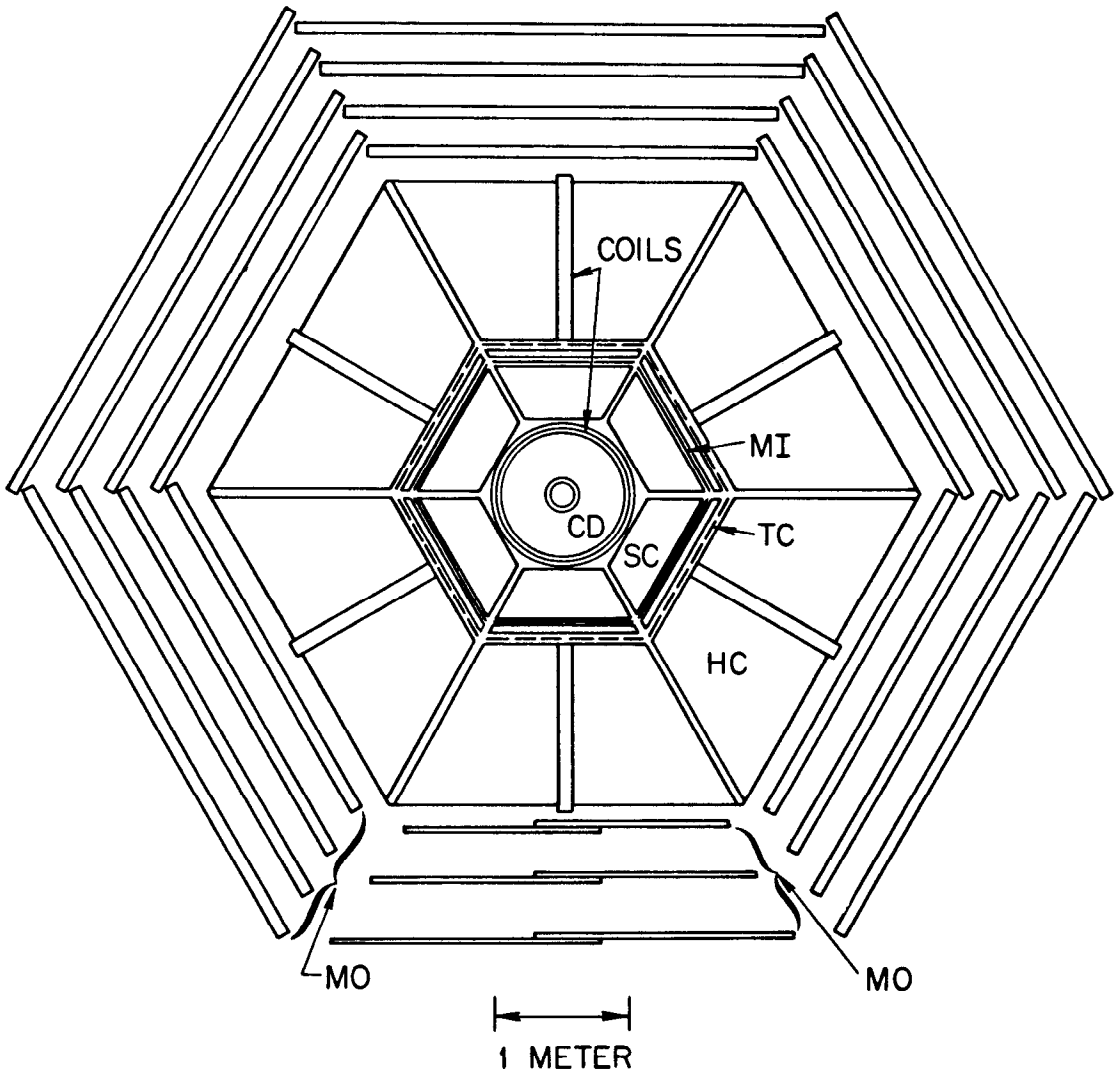

Figure 3–1: The MAC detector (end view).

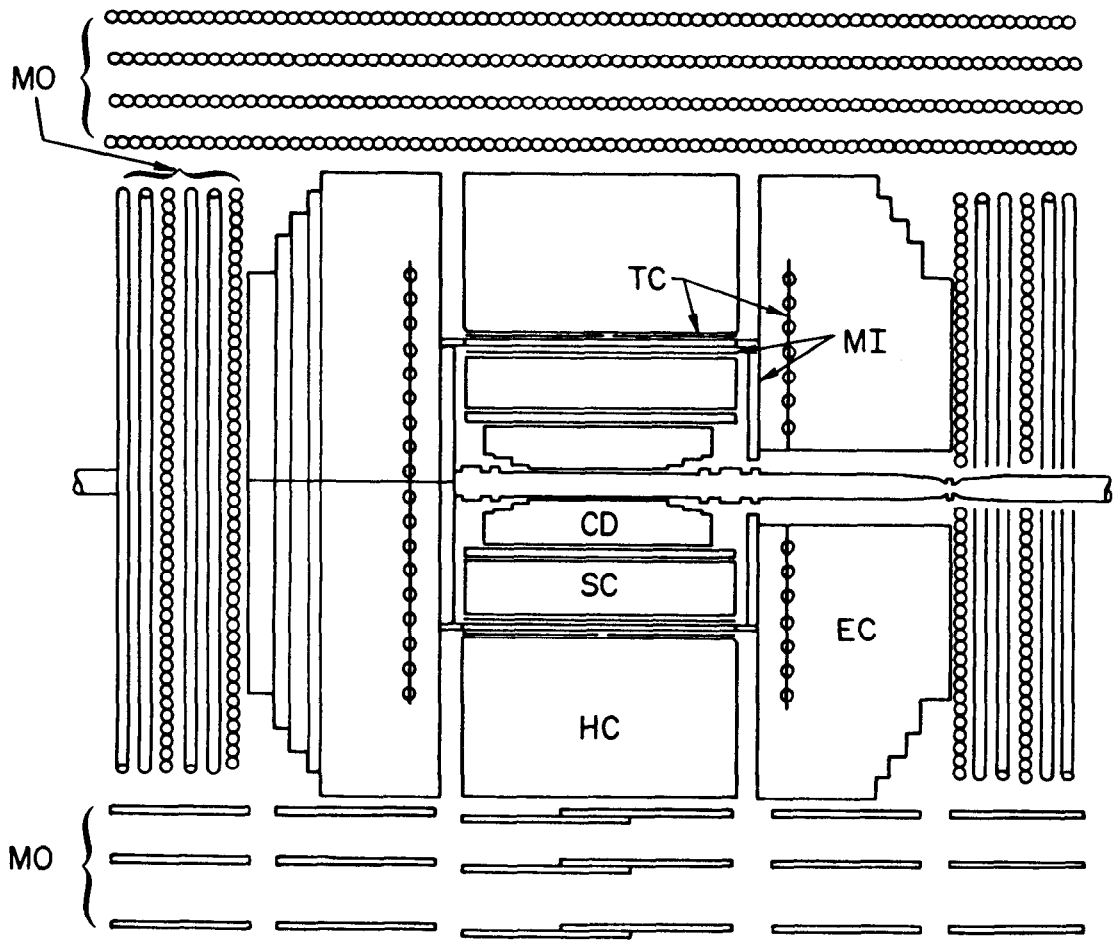

Figure 3–2: The MAC detector (side view).

12 cm and the outermost at 45 cm. Each cell runs the length of the chamber and contains two wires that enable not only the determination of the drift time, but also resolution of the ambiguity as to the side of the wire on which the particle passed. Four of the layers contain wires parallel to the z-axis, and between each pair are two layers, one askew by $+3°$ and another by $-3°$. This scheme allows the location of all three components of the position of a hit in the chamber once the track has been reconstructed. The chamber is filled with a gas mixture containing 90% argon and 10% methane.

The point measurement accuracy is about 200 μm. A solenoid magnet surrounds the drift chamber, and provides a magnetic field of 5.7 kGauss directed along the beam axis. This field enables a momentum resolution of the drift chamber obtained by the formula $\frac{\Delta p}{p} = .065 p \sin\theta$, where resolution due to angular mismeasurement has been neglected compared to the uncertainty in curvature, which is much larger. A drift cell in each of the ten layers is crossed by particles in the angular range of $23° < \theta < 157°$, but useful momentum information can still be obtained for particles in the range $17° < \theta < 163°$. Recently-installed electronics allow the recording of up to two distinct traversals in each cell per event.

The central section of the detector extends to $z = \pm 113$ cm and contains the entire inner drift chamber. On both sides, at larger values of z, are endcaps, whose design is described below.

3.2 Calorimeters

In the central part of the detector, shower chambers surround the solenoid coil. These chambers consist of 32 layers of lead, each of thickness 2.5 mm, in-

terspersed with proportional wire chambers. The total thickness of the chamber amounts to 16 radiation lengths, making it optimal for the detection of electromagnetic showers, produced by electrons and converted photons. Anode wires are suspended parallel to the z-axis, each within its own rectangular aluminum cathode measuring 1×2 cm. The geometry of the shower chambers is hexagonal with full azimuthal angle coverage and with each of the six detectors segmented into 32 azimuthal and 3 radial sectors for independent readout. The fine segmentation provides a resolution of shower centroid azimuthal position of about 1°. Both ends (positive and negative z) of each wire group are read out and the z-position of the shower centroid is determined as a function of the ratio of these measurements, the wires acting as a potential divider. Errors in determination of z are as low as 1% of the total wire length for selected Bhabha events, but the resolution worsens for showers in more complicated hadronic events. The energy resolution has been measured to be $\frac{20\%}{\sqrt{E}}$, or just over 5% for 14.5 GeV electrons.

A single layer of scintillators surrounds the shower chambers. These scintillators, 144 in number, are used in some triggers of the data-taking process and provide the necessary time-of-flight information to distinguish mu pairs created at the interaction point from cosmic rays passing through the detector.

The hadron calorimeter provides calorimetry for particles that penetrate the shower chamber. It consists of 24 steel plates of thickness 2.5 cm alternating with proportional chambers, radially outward of which are three steel plates of 10 cm thickness, providing a total of 4.3 interaction lengths of material to stop particles generated at the interaction point. Its geometry is similar to that of the shower chamber—hexagonal—and its segmentation is identical, with each sextant

having 3 layers of 32 segments. The first two layers provide the same kind of charge division readout as in the shower chamber. Two layers of propotional chambers between the three outermost, thick layers of steel are instrumented separately and have not been available for this analysis. Resolutions for the hadron calorimeter are difficult to obtain directly, as the presence of the shower chamber closer to the beam does not permit measurement of processes taking place solely in the hadron calorimeter. An indication of its resolution can be had from test beam studies, which indicated a value of $\frac{\Delta E}{E} = \frac{75\%}{\sqrt{E}}$ for normally incident pions.

The endcaps extend the solid angle subtended by calorimeters to 98% of 4π. They consist of 30 steel plates, 28 of thickness 2.5 cm and the outer 2 of thickness 10 cm, alternating with proportional counters, all perpendicular to the z-axis. Each endcap is divided into twelfths azimuthally, each pair of twelfths corresponding in shape to the hexagonal segmentation of the central section. Anode wires run perpendicular to a radius pointing to the center of the given sextant and are grouped into five radial layers and five layers in z. The cathode plates are also read out; these run radially and are grouped into five azimuthal wedges per twelfth. The first 9 planes of proportional chambers, amounting to 16 radiation lengths of material, are more finely instrumented so as to improve the reconstructed location of electromagnetic showers not wholly contained within the central shower chamber. Elsewhere, position resolution is limited by the segmentation: 5° in both polar and azimuthal angles. The energy resolution of the endcaps is highly dependent on polar angle, because of azimuthal gaps in the efficiency of the detection apparatus at polar angles near the beam pipe. For

14.5 GeV electrons in a restricted angular range, an energy resolution of 12%, or $\frac{70\%}{\sqrt{E}}$ has been attained. All of the calorimeters contain a gas mixture of 15% methane and 85% argon.

A measurement of total energy for hadronic events with most of their 29 GeV energy in the central section results in a resolution of 18%, or $\frac{100\%}{\sqrt{E}}$. Much of the error arises from fluctuations in the ratio of charged to neutral energy in hadronic events, since charged pions tend to deposit sizeable amounts of energy in both the shower chamber and the hadron calorimeter, while neutral pions generally decay in the shower chamber, whose efficiency for detecting electromagnetic showers is greater than that for hadronic showers.

3.3 Outer Drift System

The hadron calorimeter and endcap calorimeters are surrounded by a toroid coil, which provides a field of 17 kGauss directed azimuthally. Particles traversing the calorimeters in a given sextant curve in a plane containing the beam and the azimuthal center of that sextant. Particles that penetrate the $\sim$1 m of steel in the calorimeters are tracked, upon exit from the steel, by drift chambers that surround all parts of the calorimeter. Covering five of the sextants are cylindrical drift tubes that are perpendicular to both the z-axis and a radial vector pointing to the center of each sextant. The tubes have a radius of 5 cm and are arranged in 4 radial layers, each containing 88 tubes. The middle two layers are offset by 1 cm in azimuth with respect to the others to aid in resolving ambiguity as to which side of the wires the particle passed. A position resolution of about 2 mm is obtained by these cells. The momentum of muons that penetrate the calorimeters is obtained, as described in Chapter 5, by reconstructing a track in

the outer drift system, projecting it back to the interaction point, and measuring the curvature of its path through the magnetized iron.

The remaining sextant has drift layers whose location beneath the detector limits their size. Three layers of drift planes provide tracking. Particles exiting the endcaps near the beam pipe are tracked by six layers of drift tubes that determine all three components of the particle's path. Two layers have horizontal wires and the remaining four have wires slanted at $\pm 60°$, two with each sign, from the horizontal. The "endplug" chambers are not used in this analysis.

3.4 Calibration

Energies are calibrated in two ways, depending on the nature of the particles involved. For electromagnetic showers, produced by electrons and photons that convert within the detector, the observed energy spectrum of Bhabha events is used to calibrate both the central shower chamber and shower part of the endcaps. Energy lost by hadrons is detected less efficiently, so the calibration constants obtained above cannot be used except in approximate form when converted according to theoretical expectations. Actual measurement of the hadronic energy conversion constants for the various detectors is obtained by selecting those constants that yield the expected average energy for the observed hadronic sample and make the average energy independent of thrust axis angle, except for angles where loss of particles down the beam pipe is significant. These numbers are then checked for consistency with the electromagnetic constants and the values obtained by observing the spectrum of cosmic rays in the hadron calorimeters.

Chapter 4

Data Acquisition and Filtering

The fine segmentation of the MAC calorimeters results in a very large number of independent signals that must be read in for each event. The central section calorimeters alone produce 2100 separate channels of information.

Each channel is amplified and its maximum pulse height recorded by a "sample and hold" circuit. A BADC[1] (Brilliant Analog to Digital Converter) circuit is instructed, when certain triggering conditions have been met, to digitize each of the channels in sequence and transmit the voltage readings to the main online computer. The BADC's also digitize signals from the drift chambers, after the time of arrival of these pulses is converted to a voltage level. In all, six BADC's are employed in the taking of data from all calorimeters and drift chambers. The signals from the scintillators are separately read in, after both the time and pulse height of the signal have been digitized.

4.1 TRIGGERS

Three packets of electrons circulate in the PEP ring, with three "bunches" of positrons circulating in the opposite direction. With approximately 1 mile to

---

[1]M. Breidenbach, E. Frank, Jim Hall, D. Nelson, *Semi-Autonomous Controller for Data Acquisition: The Brilliant ADC.* SLAC Report SLAC-PUB-2032, 1977.

traverse in circling the ring, each bunch intercepts its opposite number at the MAC vertex every 7 μsec. As no computer could possibly sample data from each of the 400,000 beam crossings that occur each second, a fast method of selective triggering of the data-taking process must be employed.

Several independent triggers are used, the most important of which, for the analysis presented here, signals the presence of significant amounts of energy deposited in the various calorimeters. Each circuit board that performs the function of preliminary amplification of calorimetric signals before digitizing, also maintains a signal that is the sum of the pulses coming from the calorimeter. These sum pulses are added to form 9 voltage levels, corresponding to the total energy in each of the central shower chamber sextants, in the central hadron calorimeter as a whole, and in each of the two endcaps. If 2 or more of these levels is above its threshold (set at a total pulse height corresponding to about 1.5 GeV), the online computer is sent a signal indicating that it should read the BADC and scintillator data. At the same time, the "sample and hold" electronics are instructed to save the current data; otherwise, they would be overwritten by data from the next beam crossing. When the online computer has read the data, it signals the electronics to resume the sampling. The dead time, during which the electronic circuitry is not ready to take data, averages about 10%.

Other triggers use different, often independent, information to request the start of data-taking. Several of these make use of the scintillators: either by requiring scintillators on roughly opposing sides of the detector to have fired, or by requiring more than two scintillators to have fired in the detector as a whole. Another trigger requires the presence of signals in cells in the inner drift

chamber that might constitute a track, plus a fired scintillator in the region where a particle leaving such a track would have crossed the scintillator plane. Another trigger requires the presence of enough signals, in appropriately located cells, to indicate the possible presence of roughly back-to-back inner drift tracks, plus a small amount of shower energy.

The fact that these triggers rely on different parts of the detector allows the calculation of the efficiency of one trigger compared to another, which should be equivalent to the absolute efficiency if the triggers are really independent. When applied to Bhabha events in the central section, such a calculation has indicated an efficiency of 98.8% for the energy trigger, and of very close to 100% for all triggers. This very high efficiency for detecting roughly collinear, wide-angle Bhabha events enables the simple and precise measurement of the luminosity, as described in Appendix A. It is assumed that central section hadronic events, with their high probability of firing scintillators, would be triggered with an even greater efficiency.

4.2 Online Filter

The final trigger rate is maintained at about 5 Hz, which can be handled comfortably by the online computer, a VAX 11/780. The data for the triggered event are read into a buffer, where they remain until a decision as to whether to save the event on disk is made. Simple criteria are used that do not require a full analysis, as sufficient time is not available for complete reconstruction. Data that might represent a hadronic event are saved if one or more of several conditions are met. If the data-taking has been triggered because of the total energy deposited by the event, then it is saved if it has (1) 3 GeV of energy

in the central shower chamber, or (2) 10 GeV of energy on either side of the detector, or (3) 10 GeV of energy in the hadron calorimeters (central section plus the outer parts of both endcaps), or (4) any concentration of hits that form a potential track in the inner drift with a relevant scintillator fired. Additionally, if the event has a rough inner drift track with appropriate scintillator fired, it will be saved if (1) opposing central section scintillators have fired, or (2) opposing endcap scintillators have fired with minimal energy in each endcap, or (3) more than two scintillators have fired anywhere. Finally, events having any pair of opposite sextants or endcaps with a shower of at least 1.5 GeV are kept.

The VAX filter accepts about 60% of the events it analyzes, for a data logging rate of about 2 Hz. About 1600 bytes of data are logged for a typical event, with only those channels whose reading is above a preset threshold being recorded. Shortly after a data file is closed by the VAX, it is sent by cable (the "long line adaptor") to SLAC's IBM 3081 and is written on IBM disk, where it awaits analysis by the filtering program, usually within a day of its having been created. It is then written onto tape and erased from disk. Original data files are not used again unless some error or omission is discovered in the filtering software, a rare occurrence. Figure 4–1 is a diagram of the path from the event trigger to final physics analysis.

4.3 Offline Filter

The filtering is done by the offline fast filter program (FSTFLT), which makes the decision as to which events should be kept on disk for further analysis. It also adds to the event record identifying information that indicates the class of physics to which the event is likely to belong as well as important characteristics of the

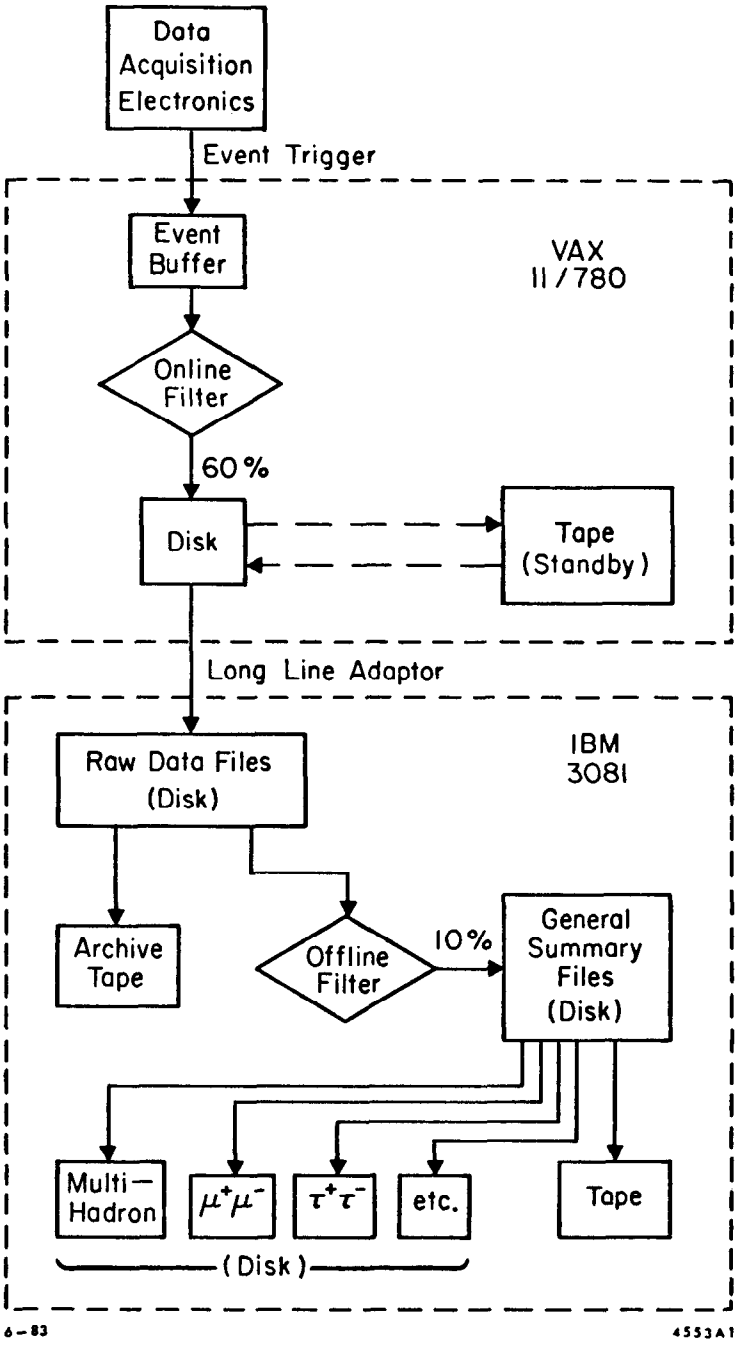

Figure 4–1: MAC data flow structure.

event, such as total energy, charged multiplicity, location within the detector, and presence and characteristics of tracks in the various parts of the detector.

The fast filter program is a three-leveled system of event selection. Events that pass the first, less time-consuming, level are passed on to the second, which is a complete reconstruction of tracks in the various detectors. All events that represent single-photon annihilation processes are meant to pass this second level, as well as many two-photon processes where significant energy was deposited in the detector. These events are all saved in disk files, which remain available on disk as long as possible, usually several months. These events are also passed on to a third level of analysis, in which various, somewhat time-consuming analyses are performed and their results stored in the event record. A typical run, containing 12000 events, takes a half-hour of CPU time in this filtering process, or 150 msec per input event. Backgrounds from non-e^+e^- sources—mostly cosmic rays, beam gas events, and detector noise—are limited to a few percent of the saved files.

The fast filter is structured in sets of "masks",[2] each of which is a set of criteria which, if satisfied, allow the event to pass on to the next level of processing. At each level, the required analysis is done for the event, and a set of as many as 18 attributes (for example, the shower chamber energy or number of inner drift tracks) is established for the event. Each mask contains an upper or lower limit (or a requirement of truth or falsehood) for each attribute, or it ignores the attribute entirely. Each of the criteria established in the mask must be met in order for the event to pass the mask, but the criteria of only one mask need be satisfied in order for the event to be passed onto the next

---

[2]The complete mask structure is detailed in Appendix B.

level of analysis. In practice, the masks are considered one at a time, and each criterion is compared with the relevant attribute of the event. If the event fails any criterion of a mask, the mask is abandoned and the next mask attempted. Time-consuming analyses, such as full reconstruction of inner drift tracks, are not done until they are needed; that is, until all other requirements of a mask needing the information have been met.

Development of the fast filter has been evolutionary. In initial running, backgrounds were high, due in large part to poor shielding, occasionally noisy electronics, and poor steering of the beam. For this reason, masks were carefully designed to be as efficient as possible at passing a set of hand-selected annihilation events, without using up precious disk space by allowing large numbers of background events to pass. As the backgrounds decreased and became better understood, it became possible to write looser, simpler, and more general masks that would allow nearly all single-photon events to be retained while still keeping the backgrounds low.

But because of the usefulness of the early masks both as familiar tags of event categories and as avenues largely independent of newer masks, the old masks have been retained, providing for a rather complicated set of quantities and cuts to be understood. Fortunately, for the present purpose, the old hadronic masks can be given a cursory treatment and emphasis placed upon the simpler masks at each level that accept higher-multiplicity events.

The most general mask at the first level requires that the total energy deposited in all calorimeters be between beam energy and 3.5 times the beam energy. It also rejects events with unphysically large numbers of inner drift hits,

as do all first-level masks; such a symptom is indicative of a hardware failure and can waste large amounts of computer time in attempted inner drift track reconstruction. Under normal conditions, this mask is sufficient to pass all hadronic events from single photon annihilation, except those few in which most of the energetic particles go down the beam pipe.

At the second level, a similar mask passes a large fraction of hadronic events. It has the same energy requirement of $E_{beam} < E_{total} < 3.5E_{beam}$, and in addition requires at least two well-reconstructed inner drift tracks that originate from the same vertex, usually the interaction vertex. The interaction vertex is required to be located within a reasonable volume, consistent with beam size and chamber resolution, from the region of intersection of the beams. All events meeting these simple criteria are saved in disk files.

The above pathway is available except for events whose measured energy has fluctuated or been mismeasured to be below the beam energy. In these relatively rare cases, a somewhat complicated set of masks allows most legitimate events to pass.

At the first level, the supplementary masks require various combinations of (1) a small amount of energy (generally less than half the beam energy) distributed in more than one sextant and divided between the shower chamber and hadron calorimeter in some reasonable way, (2) the firing of one or more scintillators, and (3) a minimum of anywhere from 2 to 6 tracks found in a cursory analysis of inner drift signals. The equivalent masks at the second level have similar energy and scintillator requirements, and require that there be at least 2 tracks found in a careful analysis of the inner drift, and that these tracks come from a reasonable

vertex.

At both levels of filtering, there also exist sets of masks specifically designed to pass Bhabha events, mu pairs, tau pairs, neutral hadronic events, two- and three-photon final states, radiative and mu and electron pairs, and various kinds of exotic processes predicted to yield low multiplicity events.

Chapter 5

Event Selection and Backgrounds

Hadronic events for this sample are selected by requiring that there be at least five charged prongs, total calorimetric energy greater than the beam energy, and a muon candidate as described below. The total hadronic sample numbers 25000 events and encompasses 52 pb^{-1} of running at 29 GeV center of mass energy and 2 pb^{-1} at 28 GeV. [1]

5.1 Muon Momentum Measurement

Muons in hadronic events are found by requiring an outer drift "stub" with an associated hadron calorimeter track. A typical event is shown in Figure 5–1. The outer drift provides no azimuthal information, except to identify which sextant the particle passed through. The procedure for determining the momentum is to find the projection of the track onto the plane, containing the beam, through the center of the sextant. Since the hadron and endcap calorimeters are magnetized, the momentum is determined by measuring the curvature of the particle's path through the calorimeter. This is done by using the outer drift information to locate the point of exit of the particle from the calorimeter, and finding the correct curved path, consistent with the energy loss of the particle in the iron,

---

[1]Measurement of the luminosity is discussed in Appendix A.

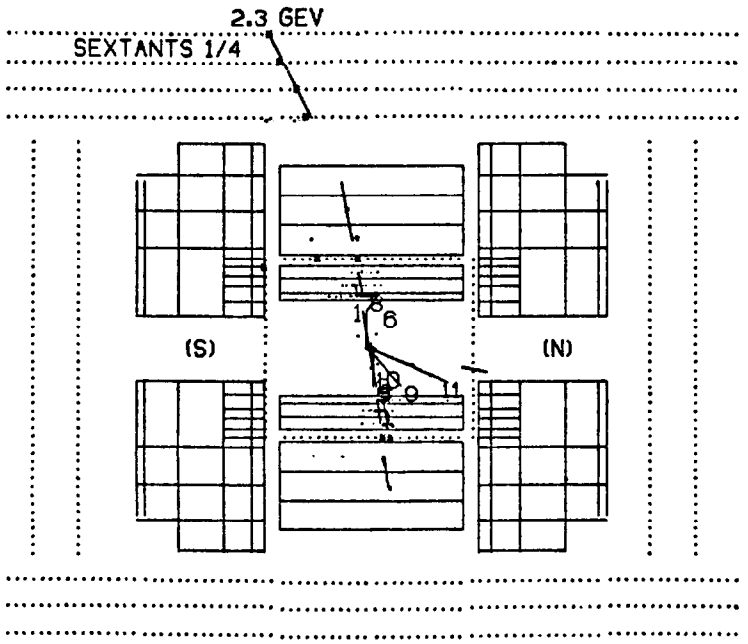

Figure 5–1: A typical inclusive muon event. In this view, the outer drift stub and associated hadron calorimeter track can be seen.

that enters the calorimeter with a trajectory that, when traced inward, intersects the main interaction vertex. Recall that the inner drift chamber is surrounded by a solenoid, so that tracks within it curve in a plane perpendicular to the beam, and therefore perpendicular to the plane of curvature in the calorimeters; so the presence of the solenoid does not complicate the projection of the track back to the vertex. After the momentum in the plane of the sextant is determined, a calorimeter track is needed to provide the third component. The axial position of entry into the calorimeter, having been determined in the momentum analysis, is used to locate the appropriate track. A track with energy in the outermost layer and an approximate match in axial position is used if such a track exists, otherwise any track whose entry location matches that of the reconstructed particle is accepted. The resolution for momentum measurement is $\frac{\Delta p}{p} = 30\%$, approximately independent of momentum, with most of the error due to multiple scattering of the muon in the calorimeters.

Once the path of the particle through the entire detector is determined, it is easy to search through the reconstructed inner drift tracks, make the best match of angle and charge, and obtain the momentum of the particle as measured independently in the solenoid field. For particles with momenta of 4 GeV/c, the average momentum of the particles in this analysis, the optimal inner drift momentum resolution of about 26% is slightly less than that of the measurement in the toroid field, but the inner drift reconstruction does not perform at its best when many highly curved tracks are present. Because the inner drift reconstruction, on occasion, groups hits incorrectly into tracks, the momentum resolution can be much worse than the quoted value in a hadronic event. While employing

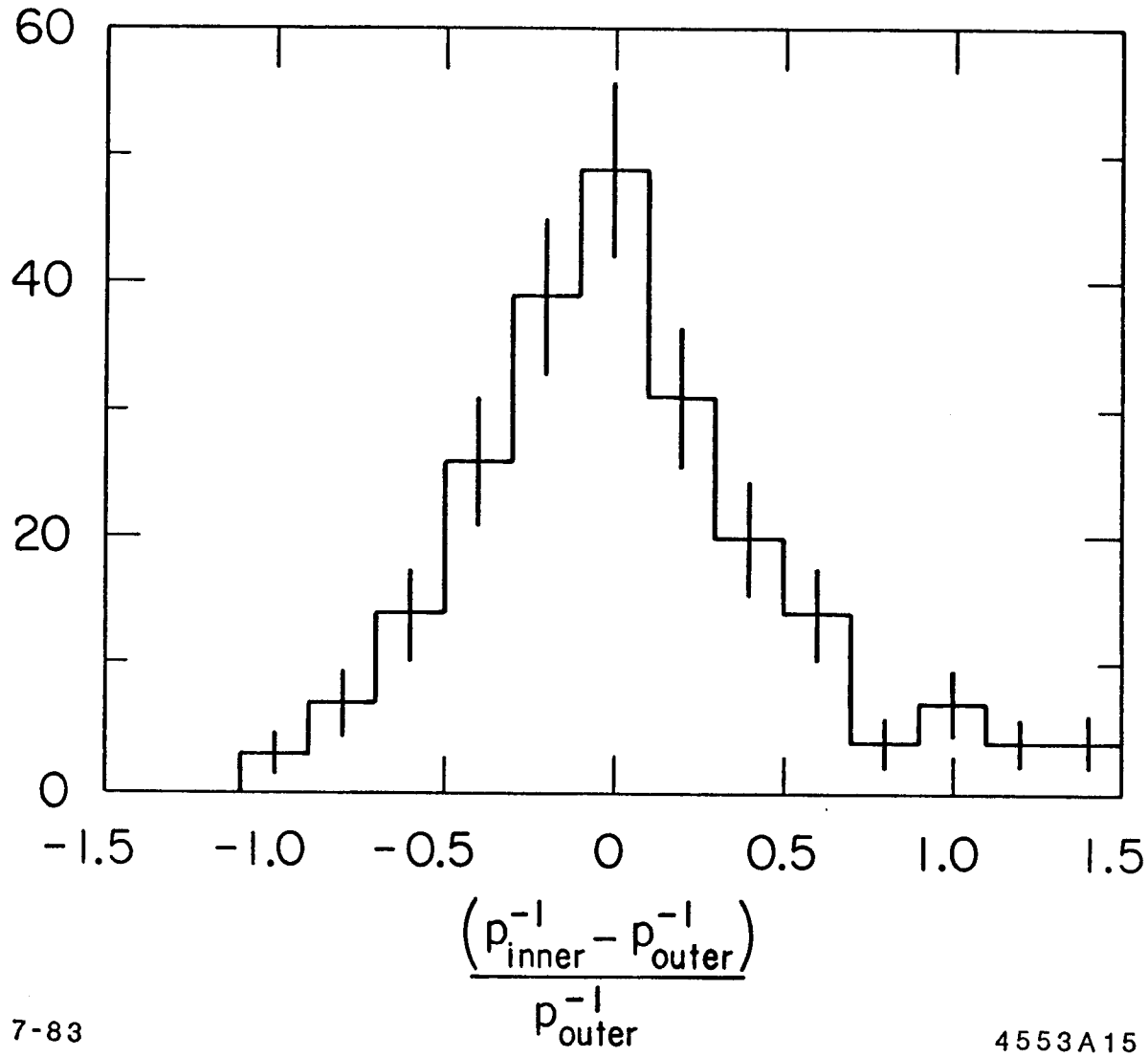

Figure 5–2: Distribution of $(p^{-1}_{inner} - p^{-1}_{outer})/p^{-1}_{outer}$, where "inner" and "outer" refer to measurements made using the inner and outer drift chamber, respectively.

some criterion as to the agreement of the two momentum measurements might eliminate such cases and possibly some of the non-muonic background, inefficiency, biased according to the density of the jet, would be introduced into the analysis in a way that is not easily modeled or corrected. The inner drift momenta are therefore not used in this analysis, but serve to verify that reasonable agreement can be obtained between the two methods of momentum determination. Figure 5–2 shows the distribution of the fractional difference between the two measurements of $\frac{1}{p}$, for tracks in which good angular agreement was achieved between the projected outer drift track and the inner drift track. The reciprocal momentum is used because its error is more nearly gaussian than that of the momentum. The standard deviation of the distribution is close to the 40% value expected from adding the two resolutions in quadrature.

5.2 Background Reduction

There are two main sources of background for this analysis: hadronic "punch-through", and the decay within the detector of pions or kaons to muons. The process known as punch-through occurs when hadronic cascades occasionally traverse the entire length of iron in the calorimeters. The low energy particles from this process that produce stubs in the outer drift layers and are misidentified as muons are distributed over a wide range of angles with respect to the incident hadron direction. Generally, the path that is reconstructed will have considerably more curvature that a muon with the same initial momentum, so these particles will generally be assigned low momenta. It is therefore required that the reconstructed initial momentum of the particle be at least 2 GeV/c, which sharply reduces the punch-through background.

The process $e^+e^- \rightarrow \tau^+\tau^-$ can be used to gain an understanding of punch-through. Tau leptons decay[2] 49% of the time to a single charged hadron, any number of neutral hadrons, and a neutrino; 15% to three charged hadrons, neutrals, and a neutrino; and 18% to each of the other two leptons, plus two neutrinos. The subset of events in which at least one τ has decayed to hadrons provides a convenient, pure source of energetic hadrons with which to examine punch-through. The only possible confusion arises from the possible misidentification of a hadronic event as a τ-pair with three charged tracks on both sides, so only events with four and fewer tracks have been used.

A study of τ decay hadrons indicates the need to eliminate tracks whose path through the detector traverses insufficient iron to reduce adequately the probability for punch-through. Whether a candidate is to be eliminated is determined by the location of exit of the particle from the calorimeters: it is removed from the sample if it exited either endcap in a region close to the gap separating the endcap from the central section of the detector. The eliminated regions subtend about 20% of the total solid angle. About one-third of the inclusive muon sample is eliminated by this cut.

The τ-pair sample also reveals a signature for many of the hadrons that penetrate the steel layers: a haze of extra outer drift wires having fired near the reconstructed stub. In many cases, punch-through seems to occur in late-developing showers, when several low-energy particles escape the detector at once. For this reason, a scan of the inclusive muon candidate sample is performed

---

[2]Results from the MAC detector on τ decays are summarized in D. M. Ritson, SLAC-PUB-2986, 1982.

to eliminate events with this signature. This process reduces the size of the sample by 17%.

The track of the particle through the hadron calorimeter or endcap is also examined to verify that it is characteristic of a muon. Some candidates (5%) are rejected because the calorimeter track to which the outer drift stub has linked has more than two segments hit in the outermost layer of calorimetry. As explained above, most punch-through contamination is expected to reconstruct with low momentum, and it is found that of muon candidates with momenta below 1.5 GeV/c, 22% have such hadron-like tracks.

The 2 GeV/c momentum cut also strongly reduces the contamination to the sample from the other principal background, π and K decay. Not only do most mesons in hadronic events at this energy have momenta below 2 GeV/c, but because of time dilation, these particles become less likely to decay, before losing energy, as they become more energetic. Unfortunately, most of the particles that decay to a muon energetic enough to penetrate the calorimetry do so before depositing enough energy to be identified in the shower chamber as a hadron, and therefore cannot be distinguished from prompt muons. The 'kink' produced by the decay is in general insufficient to serve as a signature of the decay.

The principal sources of background having been reduced as much as possible, the sample is finally scanned to eliminate a few non-hadronic events. Occasionally, cosmic rays with air showers will penetrate the detector in such a way as to mimic hadronic events, but these are relatively easy to recognize by their peculiar pattern. The final sample contains 476 inclusive muon candidate events.

5.3 EFFICIENCY

In order to compare the spectra of these events with theoretical predictions, it is necessary to determine the efficiency for identification of muons. The overall efficiency is computed by performing an analysis on events of the class $e^+e^- \rightarrow \mu^+\mu$ similar to the one described above. Since the μ-pair sample is obtained independently of the outer drift chambers, it can be used to calibrate their efficiency. The sextant outer drift chambers subtend 77% of 4π or 69% of a $1 + \cos^2\theta$ distribution. Of muons within the angular range, 49.9% produce a stub that reconstructs and passes all selection criteria. The net efficiency for all muons produced with $p \geq 2$ GeV in the entire solid angle is therefore 34.5%.

When the efficiency for detecting and reconstructing outer drift stubs is considered separately from that for selecting candidate muons by the set of cuts mentioned above, it is found that the software for the cylindrical drift tubes, which cover five sextants, reconstructs 82.0% of the muons that pass through at least three layers, while for the one sextant with planar chambers, 52.1% of muons are reconstructed. The lower efficiency of the planar chambers is due partly to gaps in the coverage (the chamber is underneath the bulk of the detector, and is therefore limited by space considerations), and partly to the fact that the chamber was not functioning during a substantial part of the running (a reconstruction efficiency of 70.1% is attained for a period during which the planar chamber was working continuously). The overall reconstruction efficiency for all sextants is 77.0%.

Once a stub has been reconstructed, it passes all selection criteria 64.9% of the time. Stubs are lost mostly through the requirement that the muon not

exit from the calorimeter too near to the "rift" between the endcap and the central section. 28.2% of muons fail this cut, 7.7% fail because they have extra associated hits in the outer drift layers, and 1.3% fail to link to an acceptable hadron calorimeter track.

5.4 Background Estimation

A determination of the level and spectra of the remaining background events is also necessary to analyze the obtained sample. To evaluate punch-through, both the τ sample and a Monte Carlo are needed. In a sample of τ events covering 28 pb^{-1} of luminosity, 5 possible punch-through events survive all the cuts that are applied to the multihadron sample. Two decay events are expected in that sample, which leaves approximately 3 punch-through events. Since the spectra of particles in the τ and multihadron samples are different, it is necessary to find a measure of the relative probability for punch-through of the two samples. Such a quantity is the level of energy in the outermost layer of calorimetry, as this is sensitive to the tail of the hadronic cascade, which is responsible for the low-energy particles that penetrate to the outer drift layers. It is found that an average multihadron event is equally likely to punch-through as an average τ event (the outermost layer energy ratio of tau to multihadron events is 1.04). Multiplying the number of observed τ punch-through events by the ratio of energies and normalizing to the correct number of events yields a prediction that $(9 \pm 7)\%$ of the final inclusive muon candidates are punch-through background events. But because of the difference in spectra and the small statistics, a Monte Carlo is used to obtain the shape of the expected momentum and transverse momentum spectra.

Because it is a much simpler process, the Monte Carlo is relied upon for both the magnitude and spectrum of the contamination from π and K decay. It is predicted that 23% of the final sample is decay background. Furthermore, this background is expected to be concentrated at low muon transverse momenta.

Chapter 6

Fragmentation and Branching Fractions

In order to compare the various experimentally obtained spectra with theoretical predictions, it is necessary to obtain certain information about the semileptonic decays of b and c quarks. The branching fractions of the quarks to muons will determine the overall number of muons in the hadronic sample. The importance of fragmentaion functions on the momentum spectrum of the muons has been described in Chapter 2. Because of the requirement that the muon momentum be at least 2 GeV/c, the number of events from each quark is also dependent on the fragmentation function.

6.1 Previous Results

Unfortunately, the branching fractions are not well determined by previous experiments. For the c quark, the branching fraction depends on the charge of the meson that the c forms. For charged D mesons, branching fractions as high as 19% have been claimed, while for D° mesons, values of about 5% have been obtained.[1] As we do not know the mixture of charged and neutral D mesons produced at this energy (this will depend on the ratio of D^{*} to D mesons

[1]W. Bacino, *et al.*, Phys. Rev. Lett. **40**, 671 (1978);
R. H. Schindler, *et al.*, Phys. Rev. **D24**, 78 (1981).

created, which is not well determined), we know only that the overall fraction is between the two extremes. Other experiments at the energy of this analysis quote a fraction, but since the result is highly dependent on fragmentation, and fragmentation has been fixed or approximated in these measurements, the results are not especially reliable. The semileptonic branching fraction for mesons containing the *b* quark has been measured, but only with the mixture of charged and neutral mesons available at threshold energies. It is not known whether the fraction is dependent on the charge of the meson, or whether the mixture of mesons at the energy of this analysis is the same as that at threshold, but it is expected that the branching fraction should be nearly independent of charge. The best threshold value, measured by CLEO[2] , is $(12.4 \pm 1.7 \pm 3.1)\%$.

Various experiments have reported results on *c*-quark fragmentation.[3] The best way to determine the fragmentation functions of the heavy quarks is to measure the meson momentum directly. When charged D^* mesons are created, they decay approximately 64% of the time to a neutral D meson and a charged pion. The D° meson decays approximately 2.4% of the time to a charged kaon and a charged pion. By reconstructing the momenta of the products and computing the invariant mass of combinations of the particles, the decay of a D^* is

---

[2]K. Chadwick *et al.*, Phys. Rev. **D27**, 475 (1983).
[3]H. Abramowicz *et al.*, Z. Phys. **C15**, 19 (1982);
M. Althoff *et al.*, DESY Report No. DESY 83/10, 1983;
W. B. Atwood *et al.*, SLAC Report No. SLAC-PUB-2981, 1982;
C. Bebek *et al.*, Phys. Rev. Lett. **49**, 610 (1982);
N. Ushida *et al.*, Phys. Lett. **121B**, 292 (1983);
J. M. Yelton *et al.*, Phys. Rev. Lett. **49**, 430 (1982).
For summaries of *c* fragmentation function results, see D. Schlatter, SLAC Report No. SLAC-PUB-2982 (1978); and K. Kleinknecht and B. Renk, University of Dortmund Report No. UNIDO-82/274, 1982.

identified by the difference in invariant mass between the D products and the D^* products. The Mark II, DELCO, CLEO and TASSO collaborations have used this technique, and arrive at fragmentation functions whose $<z_c>$ is between 0.5 and 0.7, although the precision of the results is limited by low statistics. Two experiments have used neutrino beams and emulsions to measure fragmentation. One (E531) measures the total energy of all of the decay products of the D's that are produced, and the other (CDHS) measures the momenta of opposite-sign dimuons from charm decay and uses a Monte Carlo procedure to reconstruct the fragmentation function.

The fragmentation function of the b is measured by only one previous experiment. Mark II, in an analysis of inclusive electron events,[4] obtains a function peaked at $z_b \approx .8$, but only one parameter is allowed to vary in the function, and the c fragmentation function is fixed in rough agreement with the above-mentioned, somewhat imprecise, experimental results.

The Monte Carlo of Ali *et al*[5] is used to obtain the predicted spectra for each quark flavor and for specified values of the fragmentation variable z. The matrix elements for the decays are well understood, and are employed by the Monte Carlo. The masses of the quarks are known precisely enough for this analysis, and the difference in mass among the possible heavy mesons can be neglected. The only uncertain decay product is the meson to which the B decays. Recent results from CLEO[6] quote an upper limit, to 90% confidence, of 10% for the

---

[4]M. E. Nelson, *et al.*, Phys. Rev. Lett. **50**, 1542 (1983).
[5]A. Ali, E. Pietarinen, and J. Willrodt, DESY Report No. DESY T-80/01, 1980.
[6]D. Andrews *et al.*, Cornell Report No. CLNS 82/547.

ratio of $b \rightarrow u$ to $b \rightarrow c$ decays. The Monte Carlo used here assumes that a D meson is produced 100% of the time.

6.2 Transverse Momentum

As mentioned in Chapter 2, the muon momentum transverse to the initial quark axis is characteristic of the mass of the parent meson. If an $e^+e^- \rightarrow q\bar{q}$ event is divided into two hemispheres, the magnitude and direction of the parent quark's momentum can be approximately determined by taking the vector sum of the momenta of the particles in each hemisphere. Experimentally, the event thrust axis[7] is used as the axis of the quark pair. The thrust is determined using vectors whose magnitude is obtained from the amount of energy deposited in a single shower in the calorimetry, and whose direction is that of the centroid of the shower with respect to the interaction vertex. The axis along which $\sum_i \left|E_{\|i}\right|$ is maximized is the thrust axis, and the value of the thrust is

$$T = \frac{\sum_i \left|E_{\|i}\right|}{\sum_i |E_i|}.$$

If the event is divided into two hemispheres, one on either side of a plane perpendicular to the thrust axis, the direction of the vector sum of the "energy vectors" in the two hemispheres can be compared to determine the detector resolution for the thrust angles. The resolution for determination of the parton axis from the measured thrust axis is found to be 6° in polar angle and 7° in azimuth.

The measured $p_\perp$ of the muon, then, is the component of the muon's mo-

---

[7]E. Farhi, Phys. Rev. Lett. **39**, 1587 (1977).

mentum, determined as described in Chapter 5, perpendicular to the event thrust axis. The magnitude of the momentum is measured with 30% resolution; the momentum direction is determined with 1° resolution in polar angle, and 2° in azimuth is a central hadron calorimeter track is available, 5° in azimuth if an endcap calorimeter track is used.

Figure 6–1 shows the $p_\perp$ distribution of muons in the sample, along with the predicted spectra for the heavy quark events and backgrounds from punch-through and π/K decay. The heavy quark spectra are normalized according to the best fit to the data, obtained as described below. The background is concentrated at low values of $p_\perp$, as is the contribution from $c\bar{c}$ events. The $b\bar{b}$ contribution is concentrated at higher values of $p_\perp$, enabling a highly enriched sample of $b\bar{b}$ events to be obtained.

6.3 The Fitting Procedure

To enable fragmentation of both charmed and bottom quarks to be measured in the same fit, both the momentum and $p_\perp$ of the muon is used. For the fit, an array of 20 elements is constructed, with 4 rows, each of which is a 5-bin momentum spectrum for a different range of muon $p_\perp$. The rows have lower limits of 0, .5, 1, and 1.5 GeV/c of $p_\perp$, and the columns have 2, 3, 4, 5, and 6 GeV/c of total momentum as lower limits.

Events generated by Monte Carlo are used to obtain the equivalent arrays for the predicted background spectra. For each of the heavy quarks, the Monte Carlo is used to obtain six separate arrays, each containing the predicted spectra for a specific range of the values of the fragmentation variable z. For the c quark, the six intervals of z equally divide the region $0 < z < 1$. For the b quark, the six

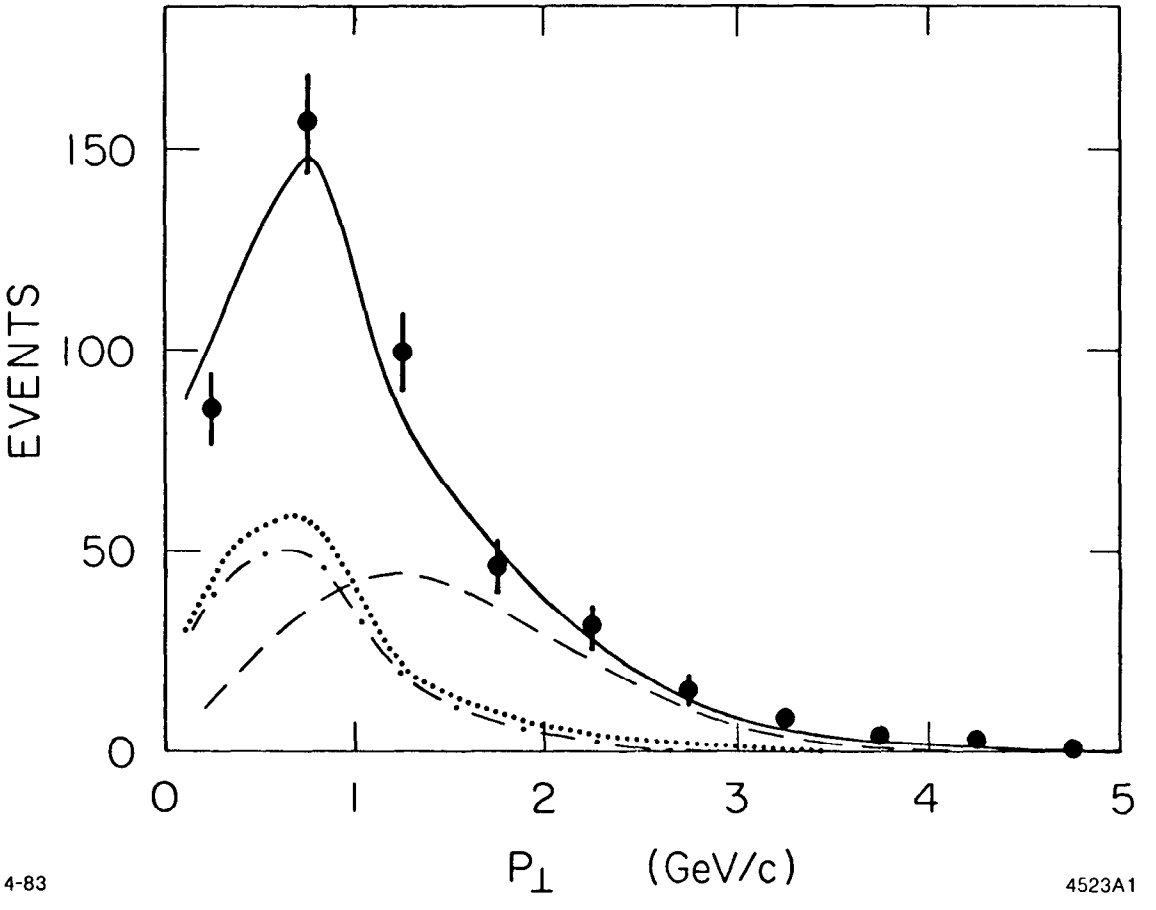

Figure 6–1: $p_\perp$ spectrum of muons with $b\bar{b}$ (dashed curve; includes $b \rightarrow c \rightarrow \mu$), $c\bar{c}$ (dot-dashed), background from decay and punch-through (dotted), and total (solid curve) predictions.

intervals divide $.4 < z < 1$; the region $z < .4$ having been found, in a separate fit, to make a negligibly small contribution to the fragmentation function.

For any given fragmentation function for quark flavor q, the average value of the function in each z interval is obtained and represented by c_k^q for the k^{th} z interval. If m_{ijk}^q is the $p_\perp$ by p array element for the i^{th} row and the j^{th} column for the k^{th} z interval of fragmentation for quark flavor q, and B_q is the overall semimuonic branching fraction for quark flavor q, then the m_{ijk}^q's are normalized so that the predicted contribution to the ij^{th} element of the $p_\perp$ by p array from quark q is

$$B_q \sum_k c_k^q m_{ijk}^q.$$

To measure the fragmentation functions and branching ratios, the c_k^q's and B_q's are allowed to vary, and the chi-square for the $p_\perp$ by p array is obtained. The c_k^q's are allowed to have any values, subject to the constraints that they are non-negative, and that the histogrammed "function" they represent normalizes to unity ($\sum_k c_k \Delta z_k = 1$) and has only one local maximum.

Figure 6–2 shows the momentum spectrum for the various ranges of $p_\perp$. The solid lines represent the best fits, with all the c_k^q's and both B_q's allowed to vary. Figure 6–3 illustrates the effect, on high $p_\perp$ events, of restricting the b fragmentation function to a narrow range of z and allowing all other parameters to vary to obtain the best fit to the entire array. It can be seen that low values of $<z_b>$ are unacceptable because of the predicted high $p_\perp$ spectrum. The spectrum is not affected by small changes in $<z_b>$ for $z \geq 0.7$.

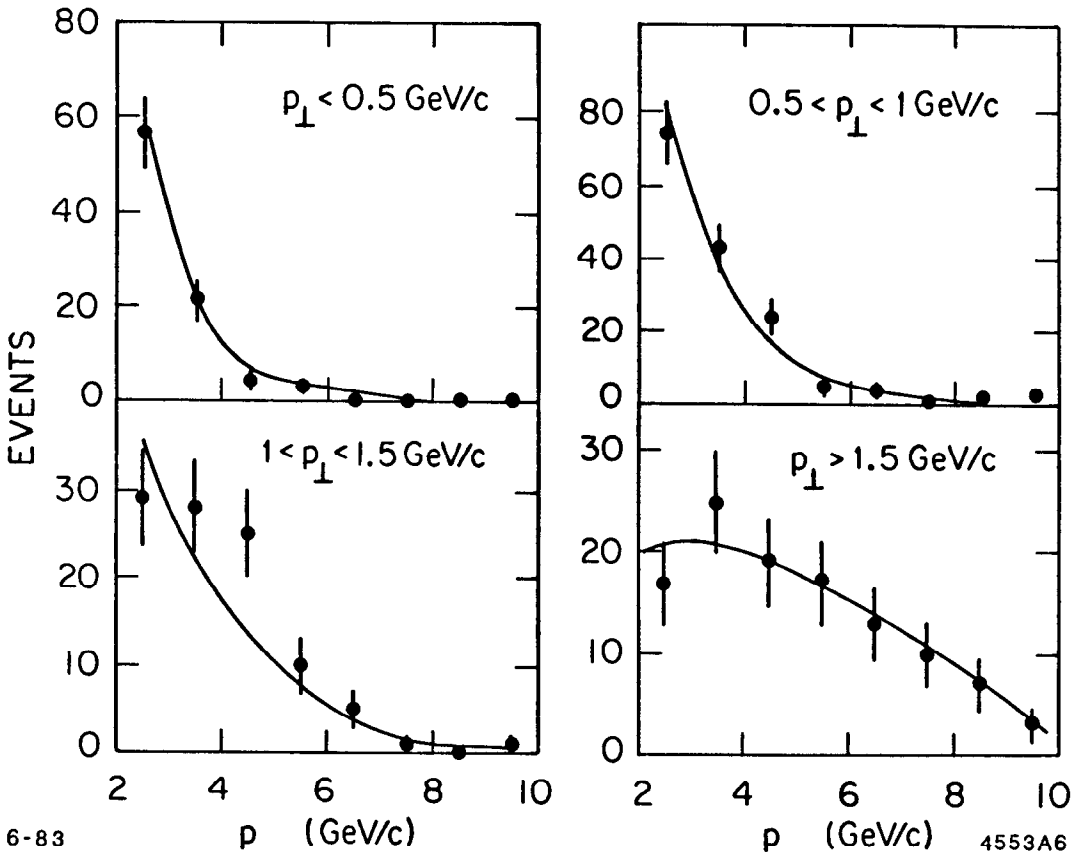

Figure 6–2: Momentum spectra for muons with various values of $p_\perp$. Solid curves are the theoretical predictions for the best fits to the fragmentation functions and semileptonic branching fractions of the *b* and *c* quarks.

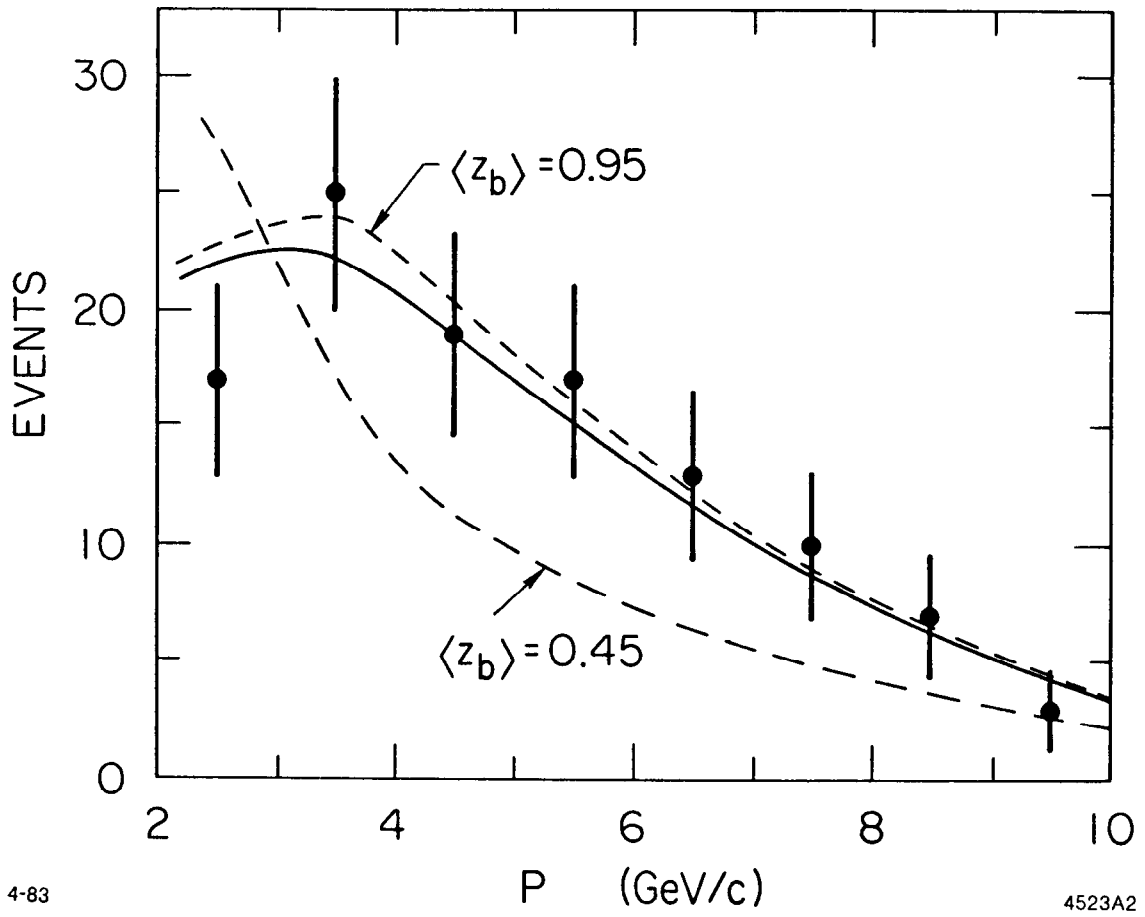

Figure 6–3: Total momentum of muons with $p_\perp > 1.5$ GeV/c. Dashed curves are the best fits obtained with the b fragmentation fixed to a narrow range of z.

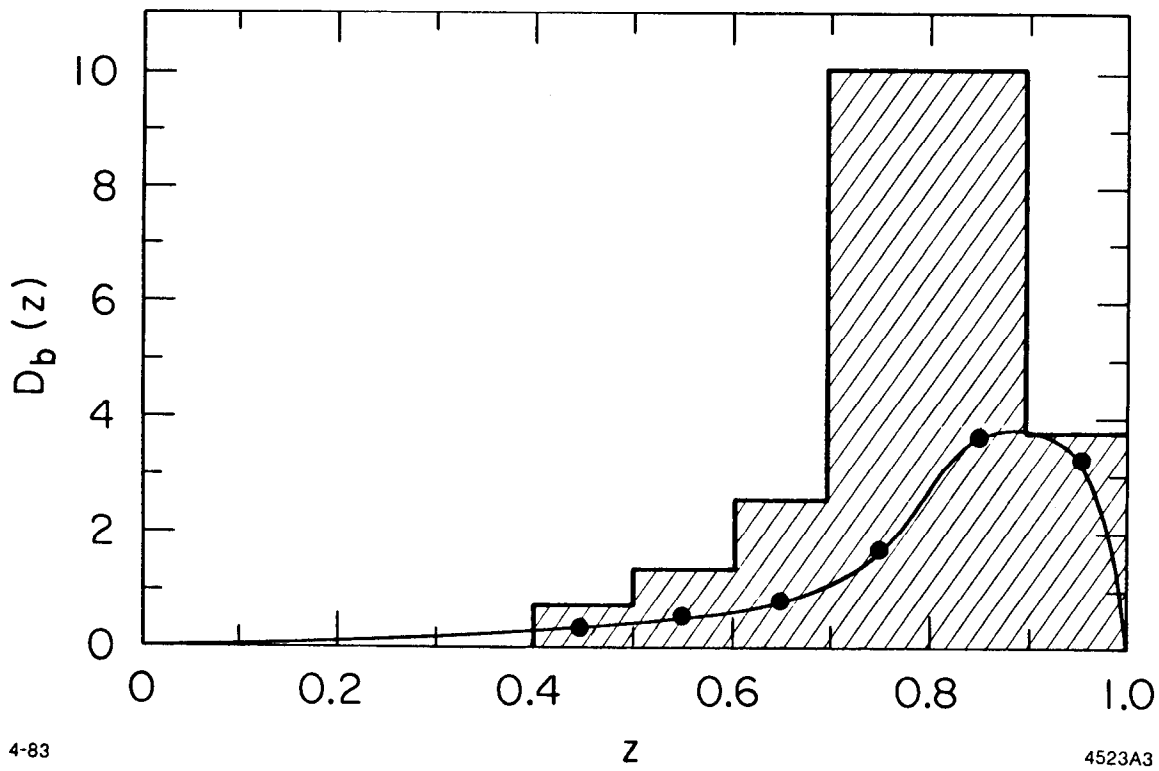

Figure 6–4: The shaded region is the envelope of acceptable b quark fragmentation functions. The curve represents the Peterson *et al.* function for $\epsilon_b = 0.008$.

6.4 Results of the Fit

The shaded region in Figure 6–4 is the one standard deviation envelope of the histograms of b fragmentation functions with spectra that yield acceptable fits. In other words, it contains the set of all histograms of properly normalized, singly-peaked functions for which the χ^2 obtained for the fit to the $p_\perp$ by p array is within one unit of the best-fit value. From the figure, it can be seen that $<z> = 0.8 \pm 0.1$. Because of the requirement that the chosen function be normalized to unity, the errors of the weights of the z intervals (the Δc_k^q's) are highly correlated, and many different functions are obtained that have values of χ^2 close to the minimum value. Such functions all have their principal contribution ($\geq 80\%$) in the interval $0.8 < z < 0.9$, and the rest in either or both of the adjacent intervals.

A particular form for the fragmentation functions has been suggested by Peterson *et al.*[8] It has

$$D_q(z) \quad \propto \quad \frac{1}{z(1-\frac{1}{z}-\frac{\epsilon_q}{1-z})^2}.$$

The fitting procedure described above is repeated, with each c_b^q set equal to the average value of the Peterson function for a given ϵ_b the the k^{th} z interval, and allowing ϵ_b, the branching fractions, and the c fragmentation function to vary to obtain the best fit. It is found that $\epsilon_b = .008^{+.032}_{-.008}$. The χ^2 for the best fit to this form is somewhat worse than for a more sharply peaked function. The errors on ϵ_b are determined by allowing the parameter to vary until the χ^2 is one

[8] C. Peterson, D. Schlatter, I. Schmitt, and P. M. Zerwas, Phys. Rev. **D27**, 105 (1983).

unit greater than this minimum value and therefore allow the function to extend beyond the shaded region in Figure 6–4.

A similar functional form, proposed by Brodsky *et al.*[9] , has

$$D_q(z) \quad \propto \quad \frac{1}{(1-\frac{1}{z}-\frac{\epsilon_q}{1-z})^2}.$$

Fitting in the same fashion as for the Peterson function, it is found that $\epsilon_b = .011^{+.054}_{-.011}$. The best fit function is almost identical to that for the Peterson function, and the χ^2 is slightly better.

A wide range of c fragmentation functions is permitted by the data. Figure 6–5 shows the one standard deviation envelope of allowed c quark fragmentation functions. Little can be concluded from the data except that $0.17 < <z_c> < 0.67$. This result is consistent with the previous results described at the beginning of this chapter.

The semimuonic branching fractions obtained in the general fitting procedure are, for the b quark (averaged over charged and neutral B mesons), $(15.5^{+5.4}_{-2.9})\%$, and for the c, $(7.6^{+9.7}_{-2.7})\%$. Both of these results are consistent with previous measurements. The c result is poorly determined because of the strong dependence of the result on the exact c fragmentation function and on the exact level of background.

---

[9]S. J. Brodsky, C. Peterson, and N. Sakai, Phys. Rev. **D23**, 2745 (1981).

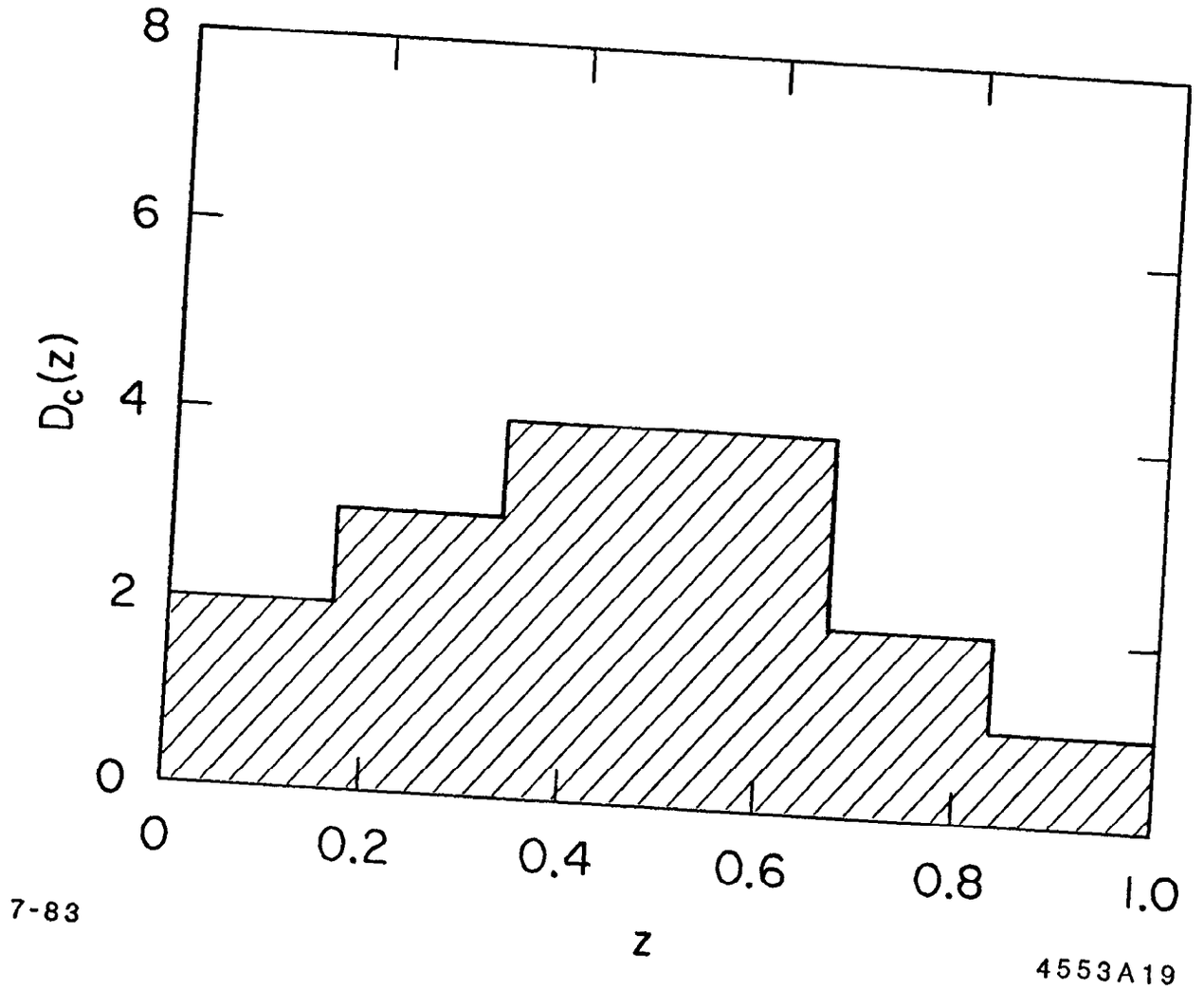

Figure 6–5: The envelope of allowed c quark fragmentation functions.

Chapter 7

The Heavy Quark Events

The predicted $p_\perp$ spectrum shown in Figure 6–1 agrees well with the data and indicates that a highly enriched sample of $b\bar{b}$ events can be obtained by cutting on $p_\perp$. Any differences that could be detected between the high $p_\perp$ sample and ordinary hadronic events might signal interesting properties of the b quark as compared to light quarks and would serve to verify the predicted large $b\bar{b}$ content of the high $p_\perp$ sample. The low $p_\perp$ sample is somewhat enriched in charmed quark events, so there is some sensitivity to the properties of charmed events as well.

7.1 Jet Invariant Mass

One characteristic expected to be sensitive to the mass of the parent particle is the total $p_\perp$ of particles in the hadronic jets. A particle that decays at rest into several approximately massless particles leaves total energy equal to its mass M in particles directed isotropically. The sum of the component of the momentum vectors of the products perpendicular to some arbitrary z-axis is represented by

$$\eta = \sum_i p_i \sin\theta_i,$$

which becomes, in the limit of a large number of particles,

$$\begin{aligned} \eta &= N \int_{\Omega} \sin\theta \, d\Omega \\ &= 2\pi N \int_{-1}^{+1} \sin\theta \, d\cos\theta \\ &= \pi^2 N, \end{aligned}$$

where N is a normalization constant, obtained by

$$\begin{aligned} M &\approx \sum_i p_i \\ &\rightarrow N \int_{\Omega} d\Omega \\ &= 4\pi N, \end{aligned}$$

$$\text{thus,} \quad N = \frac{M}{4\pi}$$

$$\text{and therefore,} \quad \eta = \frac{\pi}{4} M.$$

The mass of the parent particle of a hadronic jet can therefore be estimated by

$$M \approx \frac{4}{\pi} \sum_i p_i \sin\theta_i.$$

If the parent particle is boosted because it is created with some initial momentum, the jet mass determined above is unaffected if the z-axis is chosen to be the direction of the boost, as the $p_\perp$ of each particle is Lorentz invariant.

The 'energy vectors' described in Chapter 6 are used to approximate the momentum vectors in the above calculation. In order to separate the decay products of the two parent quarks, each event is separated into two hemispheres by a plane perpendicular to the event thrust axis. In each hemisphere, the energy vectors are summed to determine the momentum vector of the parent quark, and the $E_\perp$ of each particle is taken with respect to that axis.

Using the results obtained above, "jet mass" ("jet" is used here to mean "hemisphere," regardless of the presence or absence of gluon emission in the hemisphere) is assigned to each jet, by

$$M_{jet} = \frac{4}{\pi}\left(\frac{E_{beam}}{E_{vis}}\right)\sum_i |E_{\perp i}|,$$

where the sum is taken over all particles in the hemisphere, and $E_{vis} = \sum_i |E_i|$. The factor $\frac{E_{beam}}{E_{vis}}$, which would be unity in the case of a perfect detector of all particles, is included to minimize the effects of fluctuations in the energy measurement and of neutrinos, which are not detected. The effect of spurious noise in the detector has been reduced by the requirement that segments of calorimeter readout have a minimum energy, of approximately 100 MeV, before they are considered as forming part of a shower in the calorimeter. The detector resolution for the jet mass is about 15%, as determined by Monte Carlo calculation, for events well contained within the detector.

The hadronization process is a far more important source of distortion of the jet mass than detector effects. It is well known, for light quark events at least, that the process of creating hadrons out of quarks from the sea typically gives roughly 300 MeV of transverse momentum for each hadron. The average charged multiplicity for hadronic events, as measured by the inner drift chamber of MAC, is roughly 11, and if an additional 50% of neutral particles is assumed to be present, each jet has approximately 8 hadrons, or in the vicinity of 2.5 GeV of $p_\perp$. For light parent quarks, then, hadronization alone gives a jet mass of roughly 3 GeV and a rather broad distribution due to fluctuations in the number of hadrons created.

Gluon emission is also an important effect. If a hemisphere contains some or all of the hadrons from two primary partons (quark and gluon), the total $p_\perp$ will be large, and so will the jet mass. As α_s is large, QCD predicts that a reasonable fraction of hadronic events will contain a hard gluon jet. These will result in a large tail of the jet mass distribution at high jet mass.

Figure 7–1 shows the jet mass distribution for all jets in the entire sample of hadronic events, whose selection is described at the beginning of Chapter 5. Note the expected broad distribution, due to hadronization, and the large tail at high mass, due both to gluon emission and the presence of events with heavy parent quarks.

In the inclusive muon sample, the jet not containing the identified muon can be assumed to be independent of the jet containing the μ. Therefore, a cut can be made on the $p_\perp$ of the muon without biasing the comparison of the opposite jet with ordinary hadronic jets. Shown if Figure 7–2 is the average jet mass of non-muonic jets in the inclusive mu sample as a function of the $p_\perp$ of the muon. It can be seen that the average is greater than that for the ordinary hadronic sample only for the high $p_\perp$ (b-enriched) samples.

Figure 7–3 shows the distribution of jet mass for the jets not containing an identified muon, with muon $p_\perp$ required to be greater than 1.5 GeV/c. This is a sample highly enriched in $b\bar{b}$ events, and the distribution shows a definite shift to higher jet mass compared to the parent hadronic sample, a clear demonstration of the presence of heavy quark events in the sample.

Figure 7–4 shows the jet mass distribution for events with muon $p_\perp < 1$ GeV/c. The distribution is not particularly different from that for the overall

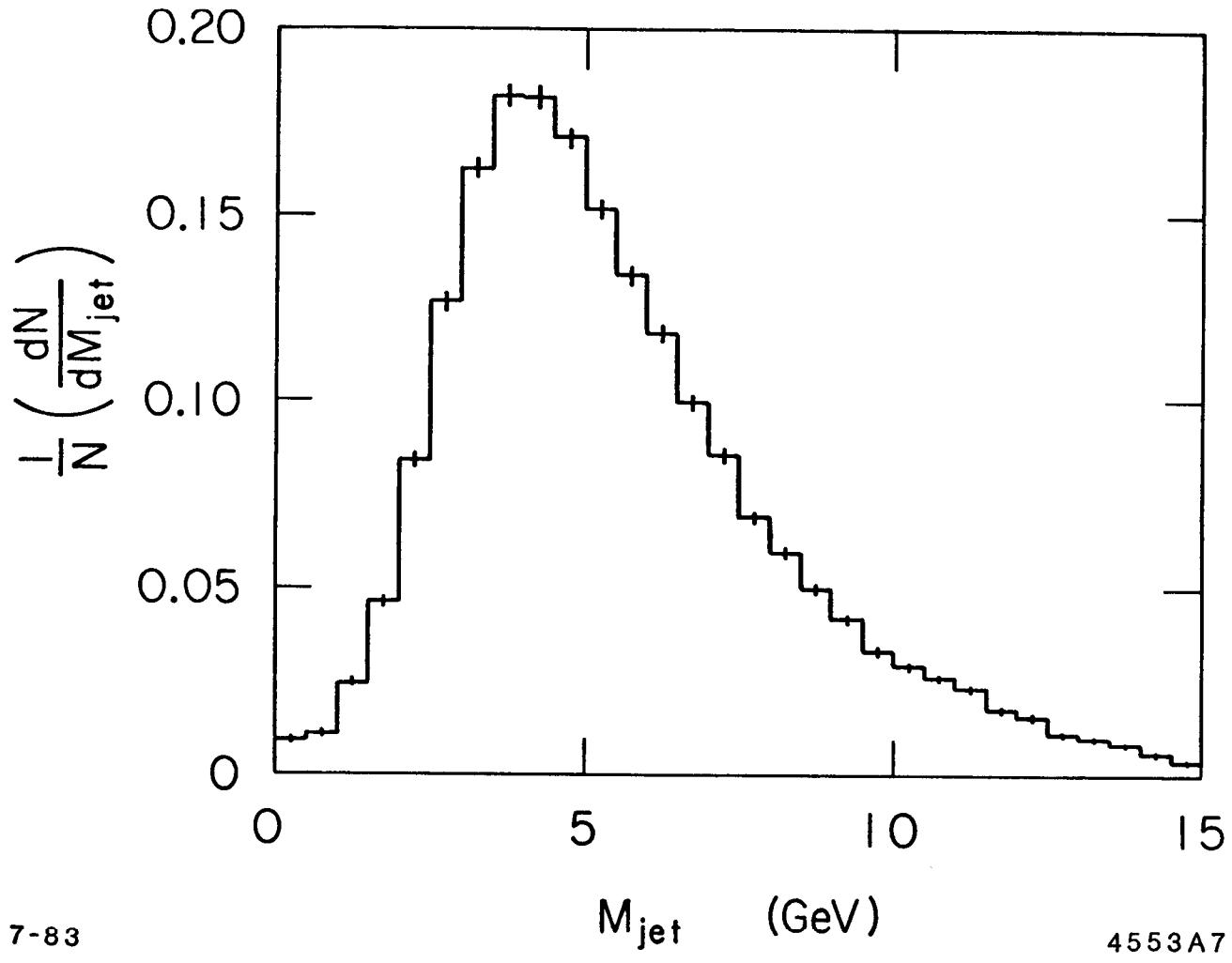

Figure 7–1: Jet mass for all jets in the general hadronic sample.

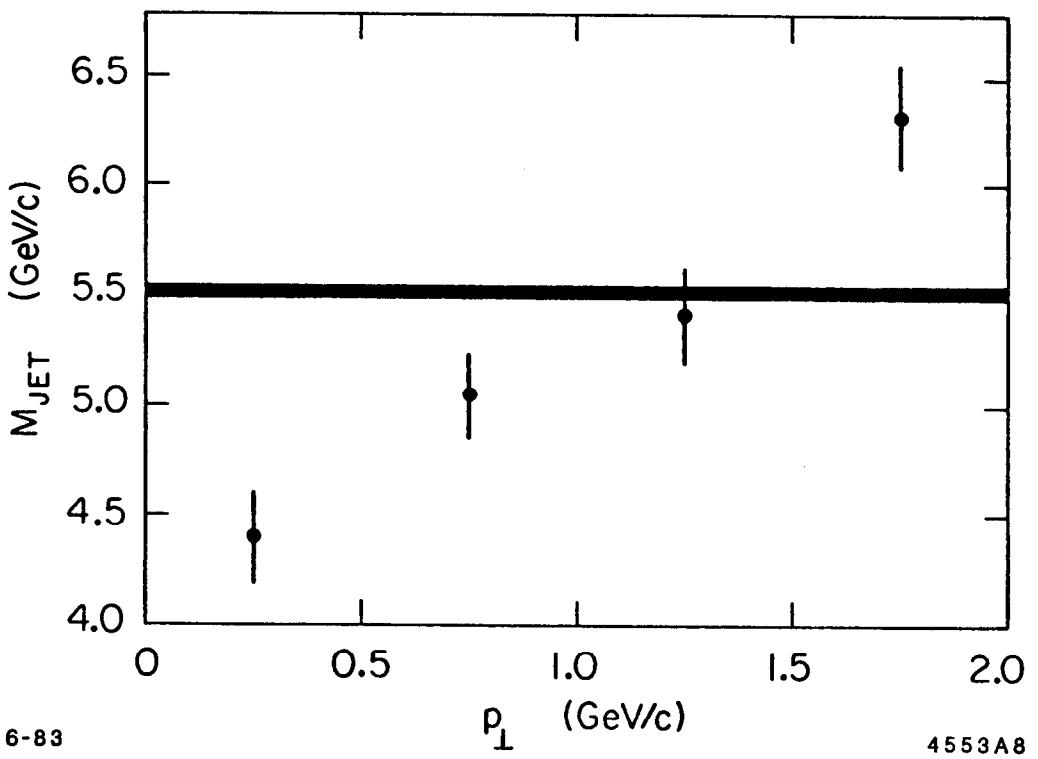

Figure 7–2: Average jet mass, of the jet not containing the muon, for various ranges of muon $p_\perp$ (last bin contains all events with muon $p_\perp >$ 1.5 GeV/c). The solid line represents the average jet mass for the general hadronic sample.

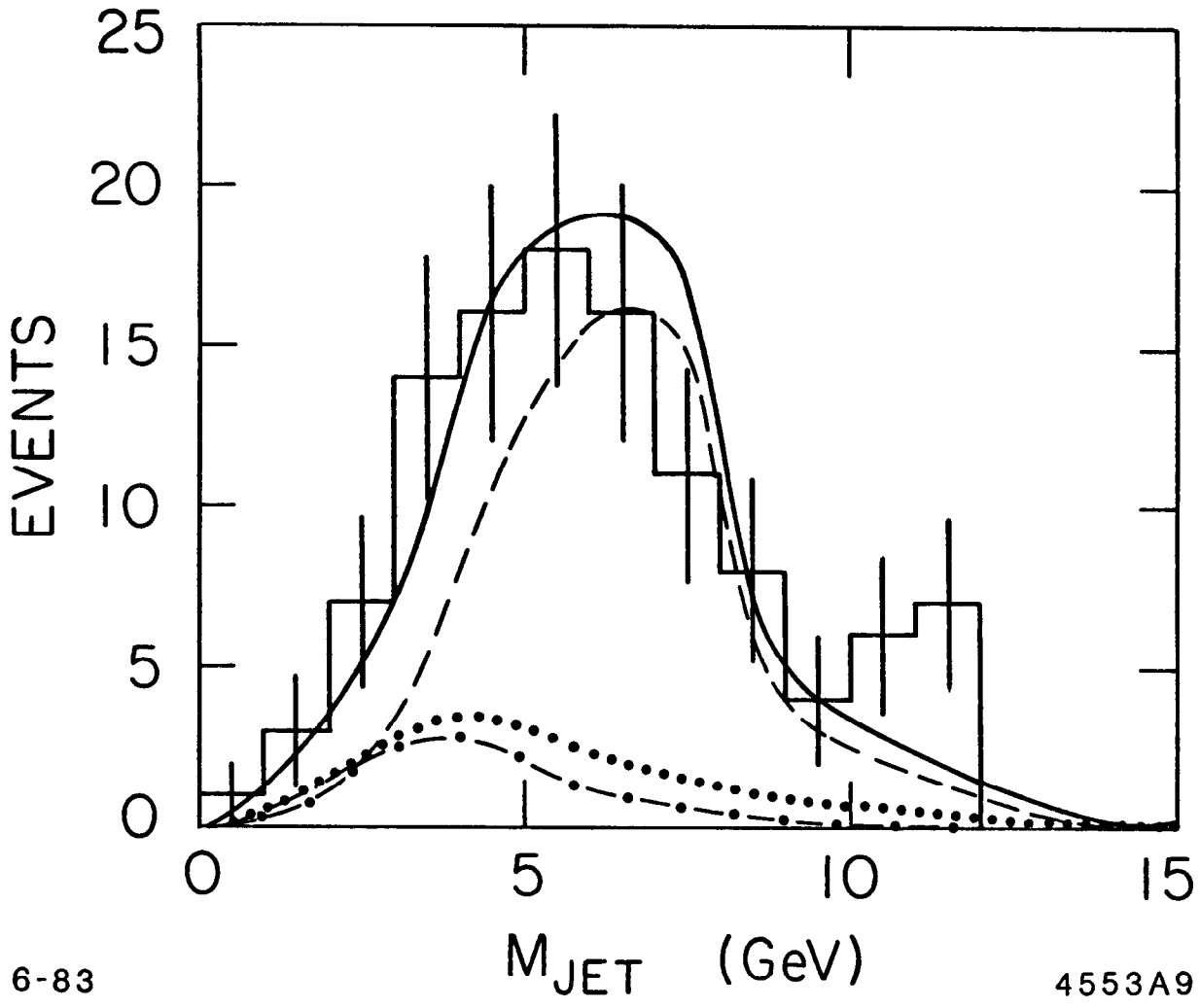

Figure 7–3: Jet mass distribution for jet opposite muon, with muon $p_\perp > 1.5$ GeV/c. Curves represent the predicted spectra for $b\bar{b}$ events (dashed), $c\bar{c}$ events (dot-dashed), background from decay and punch-through (dotted), and total (solid curve) predictions.

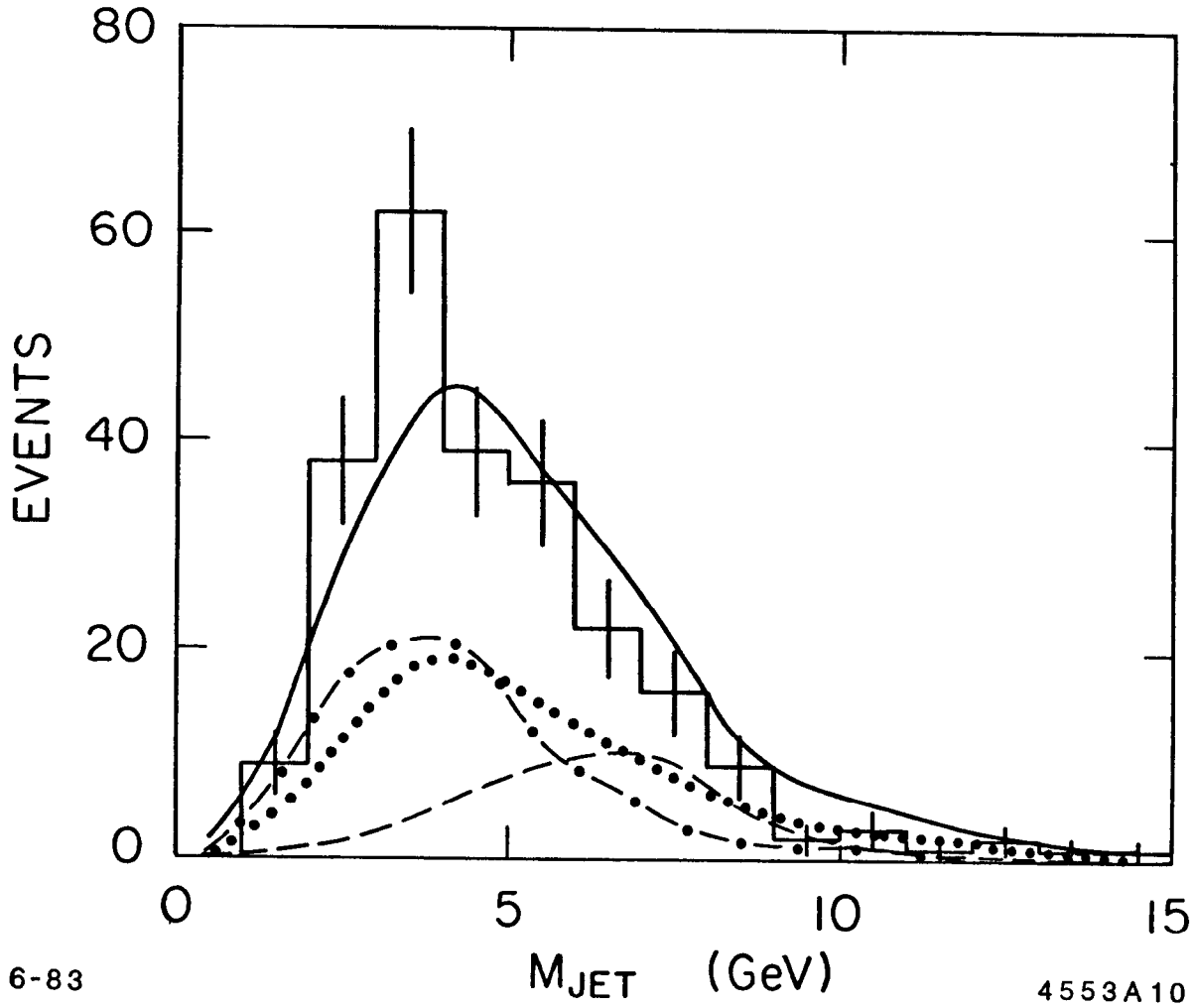

Figure 7–4: Jet mass distribution for jet opposite muon, with muon $p_\perp < 1$ GeV/c. Curves represent the predicted spectra for $b\bar{b}$ events (dashed), $c\bar{c}$ events (dot-dashed), background from decay and punch-through (dotted), and total (solid curve) predictions.

hadronic sample, except that the c-enriched (low muon $p_\perp$) events have a somewhat lower average jet mass than the general multihadron events. This may be due to a smaller hadronic multiplicity in this sample, since hadronization seems to contribute more to the jet mass than would the 1.8 GeV/c^2 mass of the c quark. Another possibility for the lower mass of the c-enriched sample is the presence of semi-leptonic decay of some ($\approx$ 20%) of the jets, which lowers the measured mass somewhat because of the missing neutrino.

One would expect that, despite the missing neutrino, the invariant mass of the jet containing the muon would be highly correlated with the muon $p_\perp$. Such a correlation is present, as shown in Figure 7–5, indicating that the masses of both jets could have been used to enrich the sample in heavy quark events, had the muon $p_\perp$ been unavailable.

There are certainly other quantities that could be used to attempt to distinguish between events according to the mass of the parent quark. Hemispheric thrust ($T_{jet} = (1/E_{vis}) \sum_i^{jet} E_i$, with E_{vis} the visible energy in the hemisphere) is one such quantity, and an alternative measure of jet invariant mass could be obtained by $E_{vis}\sqrt{1 - T_{jet}^2}$. This formulation, however, is found experimentally to be less efficient at distinguishing heavy from light quark events than the formulation used above, and more sensitive to the low energy tail of the hadronization process.

Other quantities that might be suggested make use of non-linear powers either of the particle energy or of the sine or cosine of the angle of its deposition. Since it is not always possible to divide the reconstructed calorimeter information correctly into the tracks of separate particles, all such quantities are rejected as

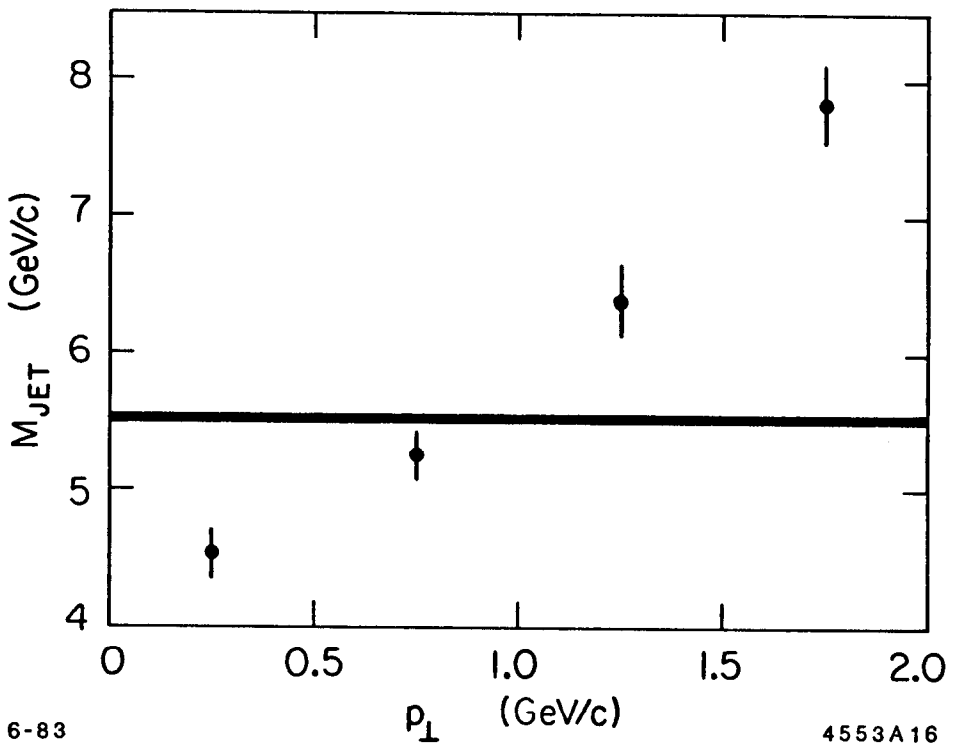

Figure 7–5: Average jet mass of the jet containing the muon, for various values of muon $p_\perp$. The solid line is the average jet mass for the general multihadron sample.

being too sensitive to the performance of the reconstruction programs and to the angular pattern of energy flow. Sphericity, for example, uses the square of the particle energy (or momentum), which means that the result is highly dependent on whether two adjacent particles are reconstructed into one or two showers.

7.2 Particle Search using the Jet Mass

The clear signature of the presence of $b\bar{b}$ events in the high $p_\perp$ sample suggests that, were there another yet-undiscovered quark with higher mass being produced, its presence would be made apparent by this method. It is already abundantly clear that the t quark has a threshold above the energy of this analysis. But had it been present, the jet mass distribution would have been radically different. Figure 7–6 shows what would be expected for a t quark of mass 10 GeV, with reasonable assumptions made as to its properties: 10% semimuonic branching fraction, hard fragmentation, and cascade decay $t \rightarrow b \rightarrow c \rightarrow s$. By the jet mass plot alone, we can rule out the t, to better than 95% confidence, at any mass up to 14 GeV.

In Chapter 2, the lack of mass predictions from QCD is lamented, and the possibility of the next quark family having its lighter quark at a mass lower than that of the t is suggested. The presence of such a quark, with charge $\frac{1}{3}$, is not entirely ruled out by resonance searches or measurements of R. Figure 7–6 also shows the effect of such a quark, with mass 10 GeV, 10% semimuonic branching fraction, hard fragmentation, and decays like those of the b (i.e., new quark $\rightarrow c \rightarrow s$). Because of its charge, it would be produced one-fourth as copiously as the t. Still, a $\frac{1}{3}$ charged quark can be ruled out on the basis of the jet mass distribution, to greater than 95% confidence, for masses between 7 and 14 GeV.

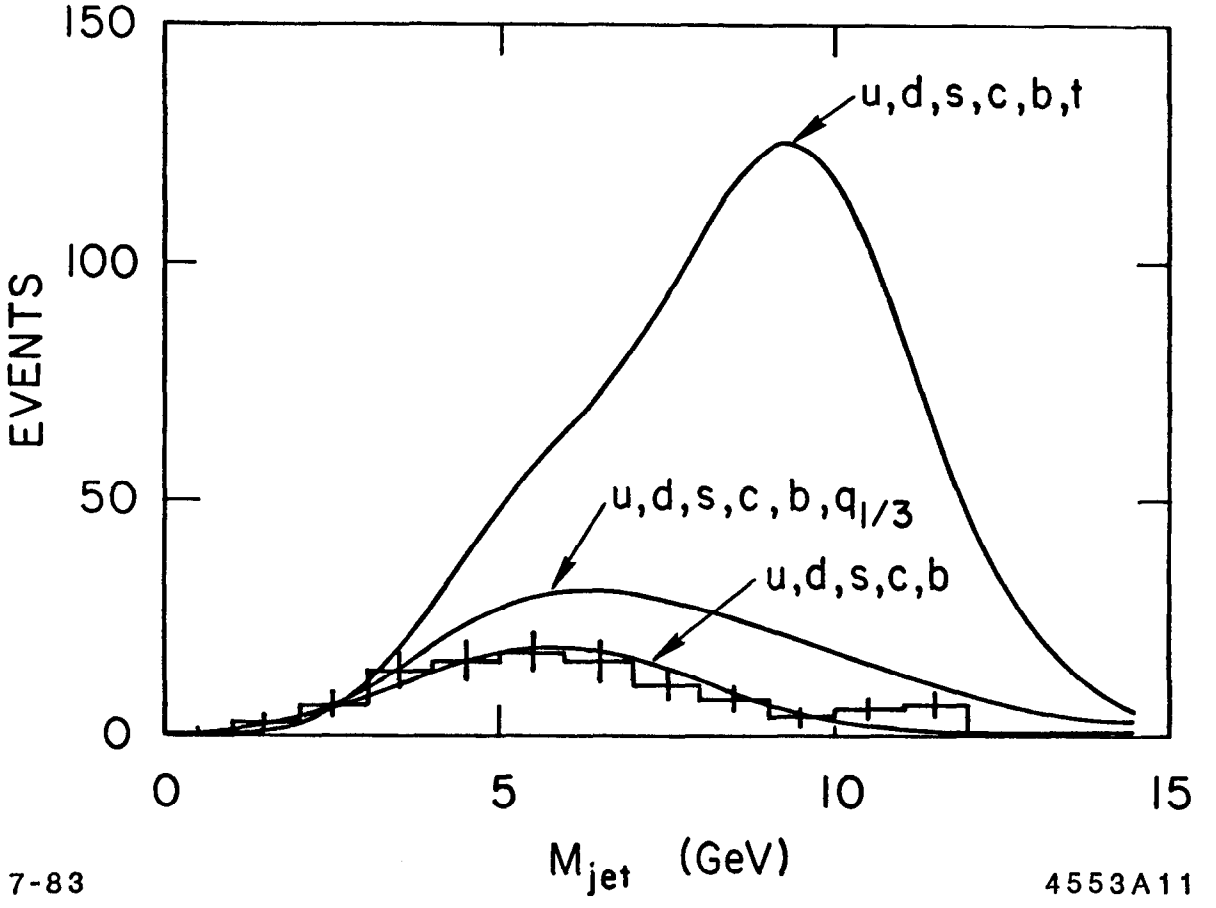

Figure 7–6: Jet mass distribution (of jet not containing muon, for events with muon $p_\perp > 1.5$ GeV/c) with predictions obtained for the usual five quarks, and for those five plus an extra $\frac{1}{3}$ or $\frac{2}{3}$ charged quark of mass 10 GeV.

In the standard electroweak model, the Higgs mechanism supplies masses to the gauge particles. At least one additional fundamental particle is necessary for this mechanism to work. If only one such particle is present, it must be neutral; but some models add additional, charged particles. In technicolor theories, technipions perform a similar function, but are composite, rather than fundamental particles. The charged Higgs particles or technipions might have a mass below the beam energy of this experiment, so that they would be produced in pairs ($e^+e^- \rightarrow H^+H^-$, where H is to be taken here and below as refering either to Higgs or technipions). If these particles were to decay to heavy quark pairs, they would contribute to the overall hadronic cross section. As they are spin-0 particles, they would be produced with a cross section of up to $\frac{1}{4}$ that of muon pairs, but this maximum cross section is not approached until the beam energy is well above the mass of the particle. For the present beam energy of 14.5 GeV and a mass of 10 GeV for the Higgs or technipion, the presence of one of these particles would add only about 2% to the number of hadronic events. This is below or comparable to the sensitivity of the high-precision R measurements expected shortly from the MAC and other collaborations. Other techniques must therefore be employed to search for these particles.

If these new particles were to decay to the heaviest available quarks ($H^+ \rightarrow \bar{b}c$), the identification of muons coming from the decay of those quarks could be used to enhance the fraction of events predicted to originate from the new particles. Starting from the total inclusive muon sample, the predicted fraction increases, for a 10 GeV Higgs, for example, if only events with one jet having a mass of greater than 10 GeV are considered. For such events, the mass of the

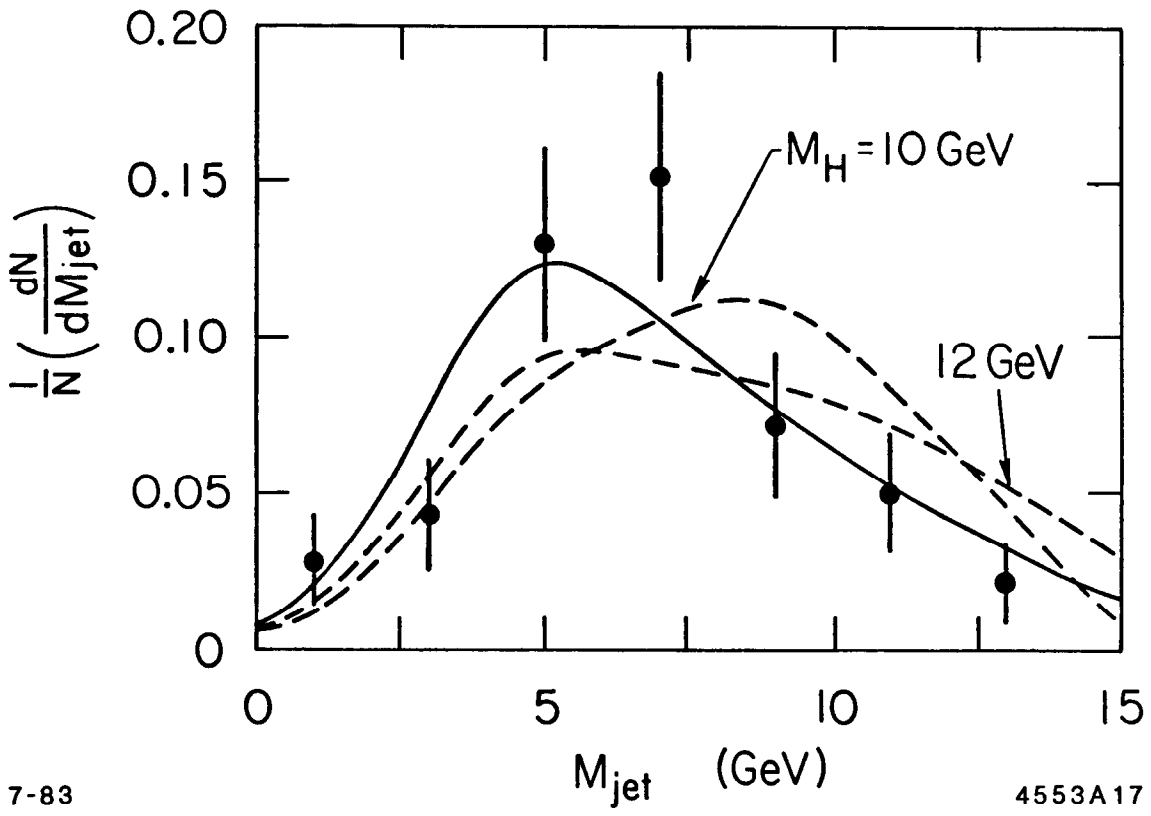

Figure 7–7: Jet mass for events whose other jet has mass $\geq$ 10 GeV. The solid curve is the same distribution for the untagged hadronic sample. The dashed curves represent the predicted spectra including a charged Higgs particle or technipion of mass 10 and 12 GeV.

other jet is displayed in Figure 7–7 along with the expected spectra with and without new spin-0 particles. As we are interested in the high-mass end of the distribution, it would be unwise to rely on a Monte Carlo calculation to predict the size of the tail of the mass distribution in the absence of new particles. As has been mentioned, this tail is principally a result of gluon emission and is therefore sensitive to the value of α_s used in the Monte Carlo. Instead, the general, untagged multihadron event sample has been used to provide a spectrum that is normalized to the observed number of events. Since the region in question is far into the tail, the increased fraction of heavy quark events in the tagged sample compared to the general hadronic sample should be unimportant, and the jet mass spectrum of the general sample should serve as a good indicator of the high-mass spectrum of the tagged events. And because the fraction of Higgs events is increased by about a factor of 4 by requiring the presence of a muon, the signature is identifyable only in that sample. To obtain the predicted spectrum with the Higgs, the Monte Carlo spectrum for Higgs events is added to a spectrum from the general hadronic sample that has been normalized so that the total number of events equals the number of observed events.

It is clear from Figure 7–7 that charged Higgs particles or technipions with masses of 10 and 12 GeV are unlikely to exist if the $\bar{b}c$ decay mode predominates. The presence of such particles can, in fact, be ruled out to greater than 95% confidence for masses between about 9 and 13 GeV by comparing the predicted and observed number of events with both jet masses above about 10 GeV.

Another possibility for the predominant decay mode is $H \rightarrow \bar{s}c$. This mode would be prefered if the particles could decay only within one family of quarks.

The present analysis cannot rule out this possibility, as the predicted number of inclusive muon events is too small.

In general, new particles would manifest themselves by a clustering in a scatterplot of the masses of the two jets. Such a plot is shown in Figure 7–8. There does not seem to be any excess of events along the diagonal at any mass above that of the b.

7.3 Charged Multiplicity

One might expect the presence of weak decays in hadronic events from heavy quarks to be signaled in some way other than by the production of leptons. The mesons containing heavy quarks decay into three particles—either a lighter meson and a quark pair, or a meson, a lepton, and a neutrino. In the semileptonic case, a sizeable fraction of the energy is carried off by particles that do not participate in the hadronization process, so it would seem reasonable that fewer hadrons would be produced by the fragmenting meson. But in the non-leptonic case, as many as three independent particles could draw extra quarks from the sea to produce hadrons, perhaps increasing the multiplicity.

These speculations suggest that, on average, the hadronic multiplicity should be higher for heavy than light quark events, and that identified semileptonic jets should have lower hadronic multiplicities than non-leptonic jets. It is difficult experimentally to separate calorimetric showers reliably into tracks of individual particles, so it is convenient to use the number of tracks in the inner drift chamber as an indicator of the overall particle multiplicity, even though only charged particles are detected. And since low-energy leptons are not distinguished from hadrons, it is reasonable to compare the total charged multiplicities of the jets.

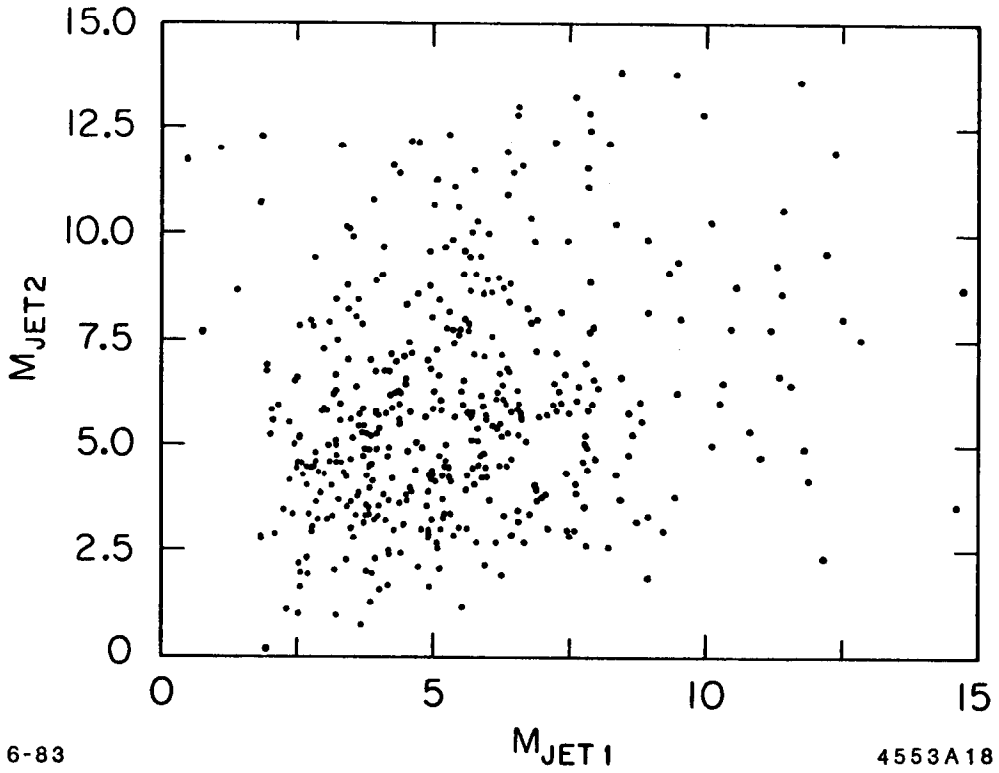

Figure 7–8: Scatterplot of the two jet masses for events in the inclusive muon sample.

The MAC inner drift chamber is small (see Chapter 3), containing only ten layers of drift cells. This number is definitely adequate for low-multiplicity events, especially τ-pairs, but is occasionally insufficient to enable correct reconstruction of all of the tracks in higher-multiplicity events. For a track to be reconstructed, signals from cells in at least 5 layers must have been recorded. In a crowded jet with many highly curving (low momentum), overlapping tracks, some tracks will be missed, some incorrectly reconstructed, and some spurious hits reconstructed into false tracks, so there is some uncertainty in the charged multiplicity measurement. Tightening of the criteria for track reconstruction would eliminate invented tracks and reduce the probability for tracks with poorly reconstructed momenta, but it would mean that tracks that overlapped other tracks would be more frequently missed. The inner drift chamber is extremely difficult to model by Monte Carlo methods, but one is generally convinced, upon scanning events, that the true charged multiplicity is generally within one track of the measured multiplicity. Energetic photons that occasionally convert to electron pairs in the beam pipe will usually add one, or sometimes two, tracks to the obtained number, which will tend to increase the measured multiplicity.

In any case, the results are presented as comparisons to the general untagged hadronic sample, which is subject to the same effects. Shown in Figure 7–9 is the average charged multiplicity of the jets not containing the identified muon, as a function of muon $p_\perp$. The highest $p_\perp$ (b-enriched) bin has a higher average charged multiplicity than the general hadronic sample by about $\frac{1}{2}$ track. No sizeable difference can be detected between the c-enriched (low $p_\perp$) bins and the general hadronic sample.

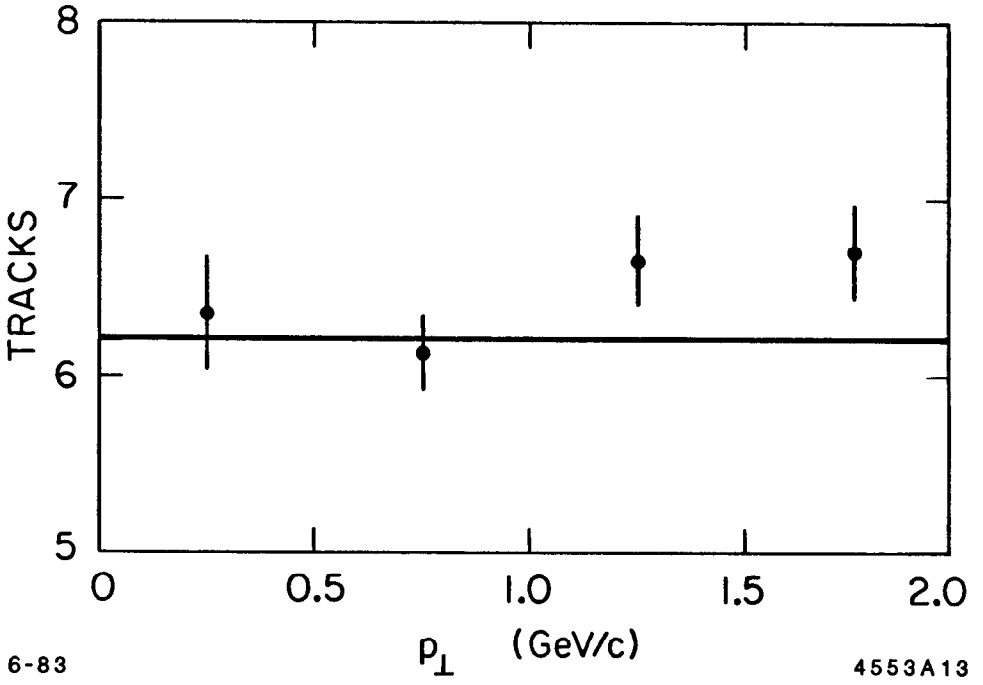

Figure 7–9: Average charged multiplicity for the jet *not* containing the muon, for various ranges of muon $p_\perp$ (last bin is $p_\perp > 1.5$ GeV/c). Solid line is the average charged multiplicity for the general hadronic sample.

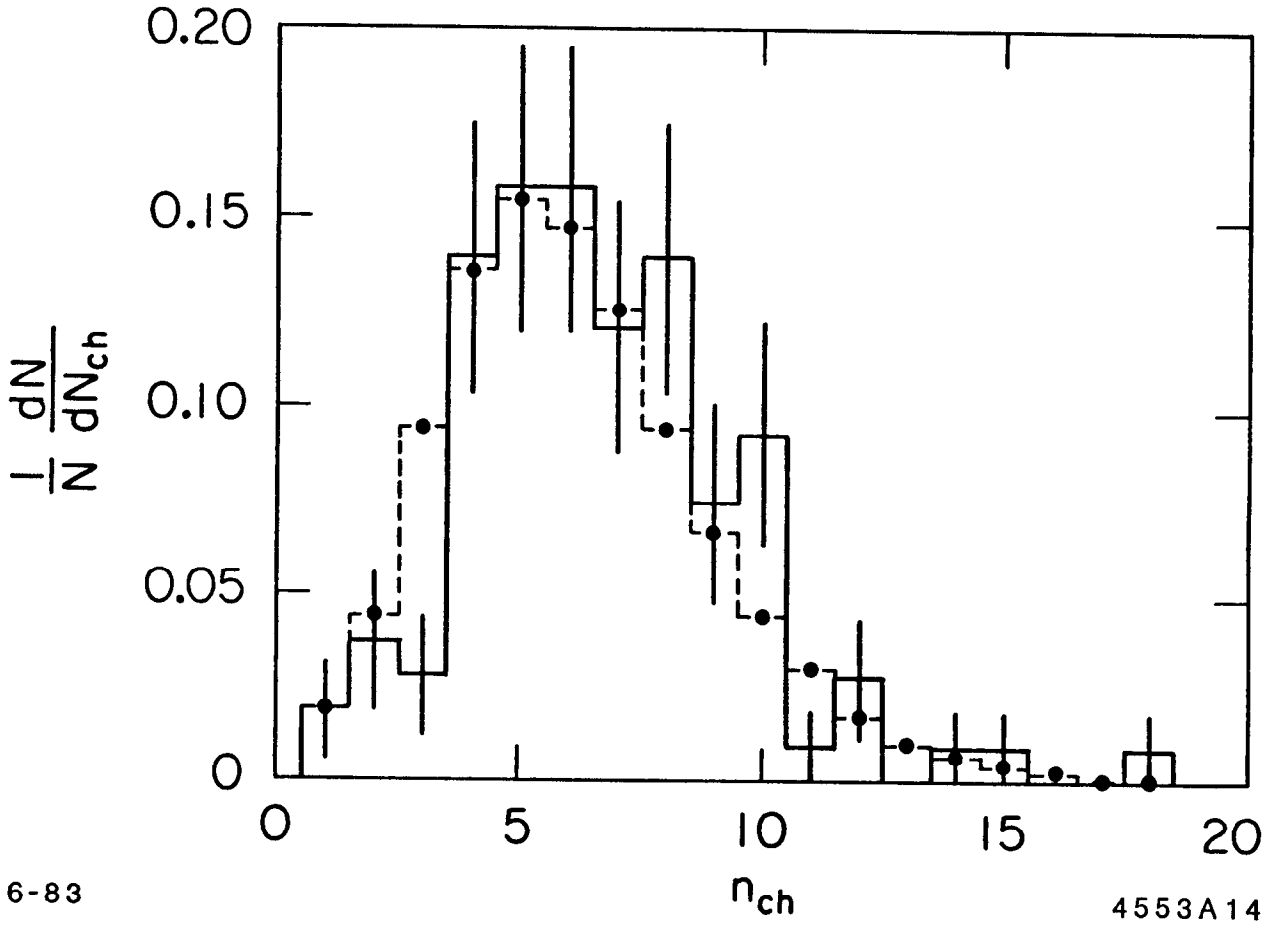

Figure 7–10: Charged multiplicity distribution for jets not containing identified muons, for muon $p_\perp > 1.5$ GeV (solid histogram) and for the general hadronic sample (dashed histogram).

Shown in Figure 7–10 is the charged multiplicity distribution for jets not containing the identified muon, for events with high $p_\perp$ muons. For comparison, the same distribution for the general hadronic sample is shown, and a general shift toward higher multiplicity can be seen in the *b*-enriched sample.

Figure 7–11 shows the average charged multiplicity for the identified semimuonic jets. It is seen that, for each $p_\perp$ bin, the semileptonic jets have lower average multiplicity than the non-leptonic jets.

7.4 Forward/Backward Asymmetry

Chapter 2 explains the prediction of the standard electroweak unification model for the asymmetry in the angular distribution of quark-antiquark pairs. It is expected that more *quarks* than antiquarks are generated in the direction of the initial *positron* momentum vector, regardless of quark flavor. The sign of the muon's charge is available in this analysis, and the sign of the charge will always be the same as that of the quark from which it decays, under the assumption that the quark into which the parent quark decays has charge of sign opposite to that of the parent quark.

For this analysis, asymmetry is redefined so that it is positive if there are more μ^+'s than μ^-'s in the *positron* direction. Since we expect more b^-'s than b^+'s ($\bar{b}$'s) in the positron direction, and more c^+'s than c^-'s ($\bar{c}$'s) in the positron direction, we expect a *negative* asymmetry for $b\bar{b}$ events and a *positive* asymmetry for $c\bar{c}$ events. The complication arises from semimuonic decays of c quarks originating from decays of b parent quarks. In this case, $\text{sign}(\mu) = \text{sign}(c) = -\text{sign}(b)$, so the expectation is for *positive* asymmetry from the relatively few muons detected from this process.

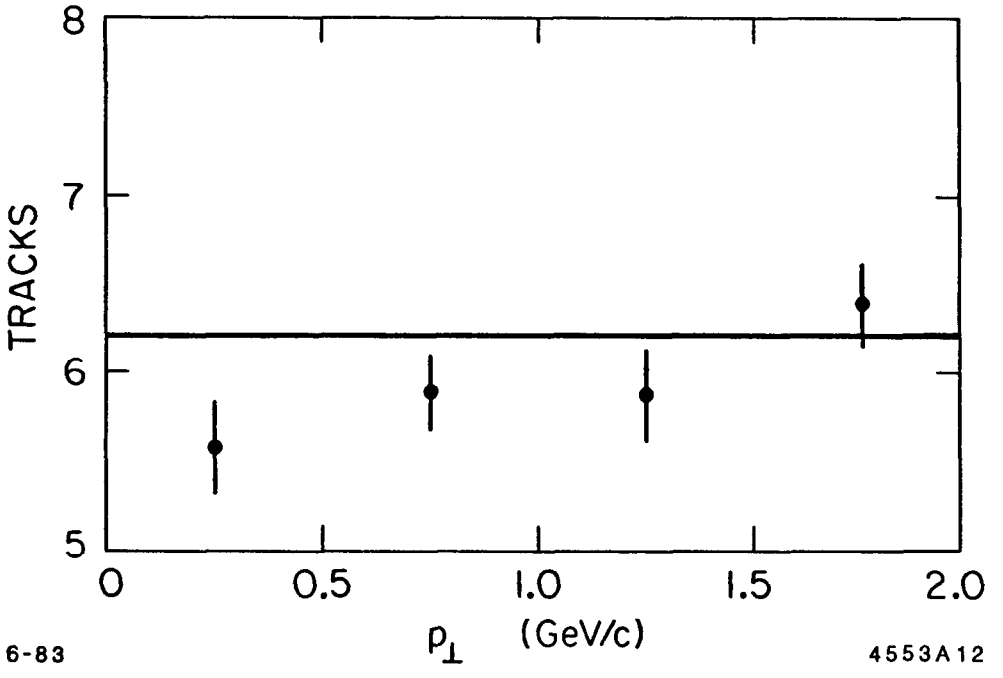

Figure 7-11: Average charged multiplicity for the jet containing the muon, for various ranges of muon $p_\perp$ (last bin is $p_\perp > 1.5$ GeV/c). Solid line is the average charged multiplicity for the general hadronic sample.

In this particular analysis, biases in selection criteria could result in a false result if, for example, μ^-'s are more efficiently selected on one side of the detector and μ^+'s on the other. A way of assuring that such effects are not present is to reverse the magnetic field in the iron, so as to cancel out any existing biases. To allow use of equal data samples with both signs of the magnetic field, additional data (collected more recently than that for the other, more complicated, measurements) are used, increasing the total exposure to 86.7 pb^{-1}.

The value of the asymmetry is determined by

$$A = \frac{\sum_i \text{sign}(\mu_i)\cos\theta_i}{\sum_i |\cos\theta_i|},$$

where θ is measured from the direction of the incident positron's momentum vector to the thrust axis in the direction of the jet containing the muon. The theoretical predictions are obtained (see Section 2.5) by the analogous integral. Table 7–1 shows the forward/backward asymmetry as defined above, for two samples, one enriched in $c\bar{c}$ events through the requirement that the muon $p_\perp$ be less than 1 GeV/c and that the invariant mass of the jet opposite muon be less than 5 GeV, and the other enriched in $b\bar{b}$ events, requiring $p_\perp > 1$ GeV/c and opposite jet mass greater than 5 GeV.

The observed asymmetry is completely consistent with the prediction of the standard model. If it is assumed that $g_A^c = -g_A^b$ and $g_A^e = -\frac{1}{2}$, then from the b-enriched sample it is found that $g_A^b = +.30 \pm .37$, to be compared with the expected value of $+\frac{1}{2}$. Under the same assumptions, the c-enriched sample indicates only that $g_A^c = -.82 \pm 1.81$, with an expected answer of $-\frac{1}{2}$.

Table 1-1: Results on forward/backward asymmetry.

Sample	$b\bar{b}$ enriched	$c\bar{c}$ enriched
Muon $p_\perp$ cut	> 1 GeV/c	< 1 GeV/c
Mass of opposite jet	> 5 GeV	< 5 GeV
Overall predicted asymmetry	-12.2%	$+3.1\%$
Observed asymmetry	$(-7.4 \pm 9.2)\%$	$(+5.1 \pm 11.2)\%$
Predicted g_A^b	$-\frac{1}{2}$	
Measured g_A^b	$-.30 \pm .37$	
Predicted g_A^c		$+\frac{1}{2}$
Measured g_A^c		$+.82 \pm 1.81$

Chapter 8

Dimuon Events

A small fraction of the events in the inclusive muon sample contain two reconstructed muon candidates that satisfy all of the selection criteria. Such events are potentially interesting, as they may reveal unexpected decays of heavy mesons to pairs of leptons, or may show unexpected charge correlations.

8.1 Expectations from Single Muon Results

A probabilistic approach is a relatively straightforward way to obtain a prediction, based on the results of the single muon analysis, for the number and character of the dimuon events. If full solid angle coverage were available and if the discussion is limited to a given flavor of primary partons, there would be little correlation between any two muons that might be produced and detected in an event, so that two probabilities for detection of a single muon in a given jet could simply be multiplied to get the dimuon probability for an event. Limited angular coverage introduces a strong correlation: detection of one muon increases the likelihood that the other potential muons in the event would be in the covered solid angle. If, however, a simple Monte Carlo calculation is used to obtain the fraction of single muons from each process that fall within the covered solid angle, the coverage factor can be removed from the probability for detec-

tion of single muons. Thus, it is possible to convert the single muon probability to an equivalent probability for the ideal case in which coverage extends over the complete solid angle. These probabilities can be multiplied to obtain the total-solid-angle probability for detection of two muons from various processes in a given event. The Monte Carlo can then be used to estimate the fraction of such events in which both muons are in the covered region. In this manner, experimentally obtained single-muon results are converted, with minimal use of the Monte Carlo, to predictions for the number of dimuon events with various characteristics.

If

$$P_r = \frac{\#\text{ muon candidates from process } r \text{ detected and passing cuts}}{\#\text{ jets in which process } r \text{ is possible}},$$

obtained from the analysis described in Chapter 6, and

$$f_r = \frac{\#\text{ muon candidates from process } r \text{ in covered solid angle}}{\#\text{ muon candidates from process } r \text{ in total solid angle}},$$

where candidates are considered only if their momentum is greater than 2 GeV/c, and a 'false muon' is a background track from hadronic punch-through or decay, then the probabilities for single muons to be produced, detected, and accepted can be summarized as follows:

Process	$P_{process}$	$f_{process}$	$P_{process}/f_{process}$
$b \to \mu$	3.15%	70%	4.51%
$b \to c \to \mu$	0.68%	70%	0.97%
$c \to \mu$	0.69%	70%	0.99%
false muon	0.30%	65%	0.46%

Table 8–1: Sources and predictions for dimuon events.

Process 1	Process 2	P_1/f_1 (%)	P_2/f_2 (%)	f_{12} (%)	P_{12} (10^{-4})	Events
$b \to \mu^-$	$\bar{b} \to \mu^+$	4.51	4.51	59	11.9	4.1
$b \to \mu^-$	$b \to c \to \mu^+$	4.51	0.97	55	2.4	0.8
c.c.	c.c.	"	"	"	"	0.8
$b \to \mu^-$	$\bar{b} \to \bar{c} \to \mu^-$	4.51	0.97	62	2.7	0.9
c.c.	c.c.	"	"	"	"	0.9
$b \to \mu^-$	false μ same jet	4.51	0.46	60	1.2	0.4
c.c.	"	"	"	"	"	0.4
$b \to c \to \mu^+$	false μ same jet	0.97	0.46	60	0.3	0.1
c.c.	"	"	"	"	"	0.1
$b \to \mu^-$	false μ other jet	4.51	0.46	61	1.3	0.4
c.c.	"	"	"	"	"	0.4
$b \to c \to \mu^+$	false μ other jet	0.97	0.46	61	0.3	0.1
c.c.	"	"	"	"	"	0.1
$c \to \mu^+$	$\bar{c} \to \mu^-$	0.99	0.99	68	0.7	0.9
$c \to \mu^+$	false μ same jet	0.99	0.46	66	0.3	0.4
c.c.	"	"	"	"	"	0.4
$c \to \mu^+$	false μ other jet	0.99	0.46	65	0.3	0.4
c.c.	"	"	"	"	"	0.4
false μ	false μ same jet	0.46	0.46	58	0.1	0.4
false μ	false μ other jet	0.46	0.46	58	0.1	0.4

Dimuon predictions must be obtained separately for each pair of possible sources of muon candidates in an event. These are shown in Table 8–1 in which P_{12} is the probability per event for observing and accepting two muons, one from process 1 and one from process 2, obtained by

$$P_{12} = \frac{P_1}{f_1}\frac{P_2}{f_2} f_{12},$$

where

$$f_{12} = \frac{\#\text{ events with muon cands. from proc. 1 \& 2 both in covered region}}{\#\text{ events with muon cands. from proc. 1 \& 2 in total solid angle}}.$$

The number of events is calculated based on a total integrated luminosity of 86.7 pb^{-1}, the same sample of events used in the asymmetry measurement of Section 7.3.

The total expected number of events is 12.8; the error assigned to this number can be neglected in comparison to the statistical error. A total of 12 $\pm$3.5 events is observed. The predicted and observed events can readily be divided according to whether the two muons have the same or opposite charge, and whether they are on the same or opposite sides of a plane perpendicular to the thrust axis. The results, presented in the table below, are in good agreement. The observed number, with its (Poisson) statistical error, is presented above the predicted number in italics.

	Same Jet	Opposite Jet
Same Charge	0 ± 1.8 *1.1*	5 ± 3.3 *2.9*
Opposite Charge	2 ± 2.6 *2.7*	5 ± 3.3 *6.1*

8.2 B^0–$\bar{B}^0$ MIXING

It has been suggested[1] that mixing might take place between the B^0 and $\bar{B}^0$ mesons, analogous to K^0–$\bar{K}^0$ mixing. If such mixing were to take place, and on a time scale short compared to the weak decays of the hadrons, the charge of the muon from the decay of neutral B and $\bar{B}$ mesons would no longer be correlated with that of the b quark. If it is assumed that $u\bar{u}$ and $d\bar{d}$ pairs are equally likely to be drawn from the sea, one of which to form a meson with the b or $\bar{b}$ quark, and that $s\bar{s}$ pairs can be neglected, then neutral B mesons should be formed half of the time. The charge correlations between opposite and same jet muons can then easily be recomputed, taking into account the loss of charge information for half of the b quark decays. The results are presented in the table below, again in comparison to the observed number of events (prediction with 100% mixing in italics).

	Same Jet	Opposite Jet
Same Charge	0 ± 1.8 *1.5*	5 ± 3.3 *4.5*
Opposite Charge	2 ± 2.6 *2.3*	5 ± 3.3 *4.5*

The observed number of events in each category is consistent with both the standard prediction without mixing and the extreme case in which mixing is complete. Unfortunately, the two cases cannot be distinguished with the present statistics.

---

[1] J. S. Hagelin, Nucl. Phys. **B193**, 123 (1981).

8.3 THE b AS A SINGLET

The failure of the top quark to manifest itself at PEP and PETRA energies has lead theoreticians to propose models in which the t is unnecessary, and the b exists not as a doublet, but a singlet. Such models predict the occurrence of decays of the b, via a flavor-changing neutral current, to a lepton pair plus an s or d quark. It has been pointed out[2] that such theories require a lower limit of

$$\frac{Br(B \rightarrow l^+l^-X)}{Br(B \rightarrow l^{\pm}X)} \geq 12\%.$$

With the semimuonic branching fraction reported in chapter 6 of about 15.5%, we must measure a dimuon branching ratio compatible with about 1.9% in order for such models to remain plausible.

The results already presented in this chapter obviously rule out a large branching fraction to dimuons, so the possible presence of dimuon decays can be viewed as a small perturbation that does not seriously affect the predictions of Table 8–1. For the 86.7 pb^{-1} of data in this sample, Monte Carlo calculations indicate that the expected number of jets in which two oppositely charged muons are observed, satisfying all selection criteria including momenta greater than 2 GeV/c, is 435 times the dimuon branching fraction $Br(B \rightarrow l^+l^-X)$, plus 2.7 jets predicted from other sources. Two such events are observed.

No dimuon production is necessary to explain the data, and an upper limit of 0.8% can be set, with 95% confidence, on the dimuon branching fraction of the b. A recent result from CLEO[3] quotes a 90% confidence limit of 0.9%; the

---

[2]G. L. Kane and M. E. Peskin, Nucl. Phys. **B195**, 29 (1982).
[3]J. Green, *et al.*, Cornell Report No. CLNS 82/547.

90% confidence limit obtained in the present analysis is 0.6%, which is somewhat lower than the CLEO result. Neither analysis permits the b quark to be in its own singlet without the t.

Chapter 9

Conclusions

As far as the data allow conclusions to be drawn, the results presented in the preceding chapters are completely consistent with our expectations, obtained from theory, other experimental results, or our own preconceptions. Nothing of importance is left unexplained and no new particles with significant semileptonic decays are present.

9.1 Fragmentation

The results on fragmentation fully confirm the postulated hard fragmentation behavior of the heavy quarks and provide a constraint that models of the hadronization process must meet. This analysis represents the first results that do not assume a specific functional form for $D_b(z)$, and the first high-statistics results using inclusive muons. It is apparent that a function that is sharply peaked near $z = .8$ is preferred by the data. The Mark II Collaboration,[1] using inclusive electrons, reports the same hard fragmentation behavior for b quarks. They obtain a sample with comparable efficiency to that of this analysis, and a somewhat larger level of background. Preliminary reports from Mark J[2] on

---

[1]M. E. Nelson, *et al.*, Phys. Rev. Lett. **50**, 1542 (1983).
[2]B. Adeva, *et al.*, MIT Report, unnumbered (1983).

inclusive muons indicate agreement with both this analysis and Mark II.

We have seen that identification of high $p_\perp$ leptons in hadronic events is a very useful method of obtaining highly enriched samples of $b\bar{b}$ events But the principal limitation of this method of studying fragmentation is that information is lost in the three-body decay of the B meson. The best information on fragmentation of the c quark has come from studies of the momentum of the D^* meson, which is identified through a signature requiring a relatively rare set of decays (see Section 6.1). Despite the very small fraction of $c\bar{c}$ events that can be identified in this way, the fragmentation measurement is improved considerably by the direct determination of the meson momentum. If an analogous signal were found for the B mesons, the b fragmentation function could be determined much more precisely, assuming high luminosity could be attained. Further theoretical work is required before the fragmentation results can be applied as a direct test of QCD.

9.2 The Jet Invariant Mass

The jet mass distribution of the inclusive muon events provides clear confirmation of the $b\bar{b}$ enrichment of the high muon $p_\perp$ sample. The distributions are found to be completely consistent with Monte Carlo predictions. The technique may also prove useful as a tool for enriching an untagged hadronic sample in $b\bar{b}$ events; the result, though not containing as high a fraction of b-quark events as the tagged sample, will contain a much larger number of such events.

The distribution has also been useful in eliminating the possibility of the existence of additional $\frac{1}{3}$ or $\frac{2}{3}$ charged quarks for much of the range of masses below the beam energy. It constitutes, perhaps, the most convincing demonstra-

tion to date of the absence of a new $-\frac{1}{3}$ charged quark. It is also found that the proposed spin-0 particles, charged Higgs bosons and technipions, cannot have masses between 9 and 13 GeV, if their predominant decay mode is to the heaviest available quarks. This result joins with other, independent results that eliminate the remaining proposed decay modes ($H \rightarrow \bar{s}c, \tau^+\tau^-$) through most of the same mass range.

As mentioned in Section 7.2, the tail of the jet mass distribution is highly sensitive to the value of α_s. The jet mass technique could, in fact, be used[3] to measure α_s both for the general hadronic sample and for the heavy quark events. Such results would test the universality of the strong coupling. Another method of comparing the couplings of different quarks is the energy-energy correlation technique.[4] Unfortunately, there is now considerable confusion as to the validity of that method's claim of a fragmentation-independent measure of α_s. It is unclear whether, as some have claimed, the measured value of α_s changes by a factor of 2 depending on whether a string or independent-jet model of fragmentation is used, or whether the situation is rectified by the inclusion of second-order terms in the theoretical prediction. In any case, it is presumed that the method will soon be better understood and, if relatively independent of hadronization particulars, will be applicable both to the tagged and untagged hadronic samples.

---

[3]D. M. Ritson, private communication.
[4]C. L. Basham, L. S. Brown, S. D. Ellis, and S. T. Love, Phys. Rev. **D17** 2298, (1978); Phys. Rev. Lett. 41 1585, (1978); and Phys. Rev. **D19** 2018, (1979)

9.3 Other Observations

The charged multiplicity distributions suggest that the presence of weak decays increases the number of hadrons produced, and that the multiplicity decreases when significant energy is carried off by leptons and neutrinos. Both of these results are consistent with our naive picture of the hadronization process.

The measurement of an asymmetry in the angular distribution of heavy quark events leads to a measurement of g_A^b that is consistent with the expected value. Unfortunately, the results are also consistent with no asymmetry being present. A much larger data sample is necessary before a firm conclusion can be reached. There are no prior published results on g_A^b with which to compare the present result.

Another measurement that promises to be significant with an increased data sample is that of the charge correlations of dimuon events. While the present sample does not permit any measurement of possible mixing in the B°–$\bar{B}^\circ$ system to be made, the analysis of Chapter 8 provides the basis for future measurements on substantially larger data samples. The overall number of dimuon events agrees with our expectation based on extrapolation from the single muon results. A study of same-jet oppositely charged muon pairs has resulted in the exclusion of the possibility that the b quark is in its own isospin singlet. This result confirms a previous result and sets an upper limit on the dimuon branching fraction of the B mesons.

Finally, inclusive muon events can also be used to measure the lifetime of mesons containing the b. Such an analysis relies on information from the inner drift chamber to locate the point of origin of the muon with respect to the primary

interaction vertex. Because inner drift tracks are required to be present and to correspond precisely in angle and momentum to the reconstructed outer drift track, the efficiency of the selection is substantially reduced. But this matching requirement allows a method of rejecting background events that was not used in the analysis reported here, so that some of the cuts used in this analysis can be relaxed. An analysis of the lifetime is being carried out by members of the MAC collaboration using a sample similar to this one with the addition of inclusive electron events. The results are expected shortly.

We have seen the wide variety of results that can be obtained by studying multihadron events that contain muons. A multitude of questions either have been answered, or are likely to be answered in the near future, by an analysis of the momentum, transverse momentum, charge, and angular distribution of the muons as well as the jet structure and multiplicity of the events. Our understanding of both the strong and the electroweak interactions will undoubtedly benefit.

Appendix A

Luminosity Measurement

The value for the integrated luminosity represented by the data of this analysis is obtained by counting the number of Bhabha events ($e^+e^- \rightarrow e^+e^-$) recorded in a restricted region of the central section of the detector, and dividing by the expected cross-section for the process, with corrections for efficiency and angular resolution.

Selection of the events to be counted is done by the offline data filter program, according to the following criteria: the event must have exactly 2 inner drift tracks and at least 5.7 GeV of energy in the shower chambers. The two tracks must be collinear, within 10° of back-to-back, and must make an angle of at least 55° with the beam axis. The axis of the event (formed by subtracting the momentum vector of one track from that of the other) must have its azimuthal angle at least 4° from the line of division between any pair of sextants. [1]

Pictures of a subsample of these events are scanned to determine the level of background in the sample, which is found to be $(1.2 \pm .8)\%$. A second sample of events with back-to-back shower energy is selected and scanned to eliminate

---

[1]The exact procedure for obtaining the luminosity sample is to search the fast-filter created disk files for events that passed the masks numbered 313, 412, and 511 (see Appendix B).

events that are not Bhabhas. The efficiency for finding exactly 2 inner drift tracks can then be measured, and is $(94.0 \pm .7)\%$. Most of the 'inefficiency' is in fact due to the conversion of a radiated photon in the beam pipe producing extra tracks in the drift chamber. This is the only filtering inefficiency: a histogram of total measured energy for these events indicates that the energy cut is well below the deposited energy of all legitimate events.

The efficiency of event triggering is found by examining the way in which the events in the pure, scanned sample of Bhabhas were triggered. Two independent sets of triggers are considered, one requiring that energy be present in significant amounts in the detector (see the total energy trigger description in Chapter 4), and the other demanding the firing of scintillators on opposite sides of the detector. Because of the independence of these triggers, the overall efficiency of one trigger can be found by looking at events that were triggered by the other. In this way, the efficiency for the energy trigger on bhabhas is found to be 98.8% (that is, 98.8% of events that fired the scintillator trigger also fired the energy trigger) and that for the scintillator trigger is 44.0% (recall that the central section scintillators are located behind the shower chamber and are not meant to detect electromagnetic showers). The probability of both these triggers failing to fire is only $.012 \times .56 = .67\%$. Additional triggers, described in Chapter 4, are also available, and it is found that $(.65 \pm .20)\%$ of events are triggered by these triggers but fail to fire both the energy and scintillator triggers. It is thus concluded that the trigger inefficiency is insignificant and no correction is made.

The cross-section for Bhabha events satisfying the above cuts is calculated

using the QED Monte Carlo of Berends and Kleiss[2] and accounting for the angular resolution of the inner drift chamber by randomly adjusting the angles of vectors generated by the Monte Carlo. The cross-section is measured to be .60 nb for $\sqrt{s} = 29$ GeV. It should be noted that only terms to order α^3 have been included in the Monte Carlo; efforts are now in progress to introduce higher order terms. Weak interaction effects are included and are of the order of a few percent.

For most of the analyses presented here, the sample of central section Bhabhas contains 26585 events, yielding a statistical error of .6%. The calculated total luminosity is then 53719 nb^{-1}, with, adding the various errors in quadrature, an error[3] of 1.81%. All of the data were taken at $\sqrt{s} = 29$ GeV except for 2043 nb^{-1} which were taken at $\sqrt{s} = 28$ GeV.

A similar analysis is performed on Bhabha events in a restricted region of the endcaps. Results of this analysis are consistent with those of the central section, within the systematic error of 5% assigned to the endcap result. The inner drift chamber performs less reliably for events with steeply dipping tracks, which do not traverse the entire ten layers of drift cells. Hope for reducing the systematic error arises from the possibility of a better model of drift chamber performance, which would enable corrections to be made for events lost due to poor measurement of track angles.

---

[2]F. A. Berends and R. Kleiss, DESY Report no. DESY 80/66 (1980), describes a similar computation.

[3]The error estimate has been increased slightly by the presence of a subset (3620 nb^{-1}) of data to which a 10% correction is applied to compensate for events lost due to a temporary trigger problem.

Appendix B

The Offline Data Filter

Chapter 3 describes the purpose and operation of the offline data filter (FSTFLT). Details of the filter's content are presented here.

A three-level structure is used, with each level composed of a set of "masks". At each of the first two levels, a set of 18 attributes is available, and each mask is made up of some combination of requirements for the values of the various attributes. The third level has masks, each composed of a requirement for the value of just one of 36 available attributes.

All input events (events logged onto disk by the VAX) are analyzed to determine whether they satisfy any first level mask. The first-level masks are presented in Table B–1. Masks numbered 111 through 115 are designed for Bhabha events (collinear electron pairs); mask 111 is also for two-gamma final states; mask 121 is for collinear muon pairs; mask 131 is for three-gamma final states; and mask 141 is an all-purpose mask for single photon annihilation events. Masks numbered 151 through 154 are for low multiplicity processes, including τ, μ, or electron pairs, regardless of collinearity; 161 through 171 pass hadronic events by requiring broadly distributed energy and/or scintillators, and a few inner drift tracks (except 171, which is for neutral hadronic events).

All events that pass any first-level mask are analyzed further and compared to the requirements of the second-level masks. Events that pass any of these masks are written onto semi-permanent disk files for later analysis by collaborators. The second-level masks are presented in Table B–2. Masks numbered 311, 313, and 314 are designed for Bhabha events; mask 312 is for two-gamma final states; mask 321 is for muon pairs; masks 331 through 335 are for acollinear electron or muon pairs, with 333 and 335 especially for $\mu\mu\gamma$ events. Mask 341 is a general-purpose mask for single-photon annihilation events with at least two prongs and 344 is for any event with at least three prongs; 343 is designed for events with a muon and at least one more prong; 342 and 345 are for events with no charged particles but broadly distributed energy, specifically, for three-photon final states and neutral hadronic events, respectively. Masks 351 through 354 are for low-multiplicity events such as τ or μ pairs; 361 through 364 are various masks to detect the widely distributed energy characteristic of a hadronic event, without heavy reliance on inner drift information; and 371 through 373 are a stricter set of hadronic masks, requiring reasonable amounts of energy not concentrated in any one part of the detector and a minimum of between 3 and 5 inner drift tracks.

It will be noted that some masks are almost identical to other masks but have stricter requirements on one or more attributes or have some additional requirements. These masks, while superfluous in the sense that they do not uniquely pass any events, are useful in that they supply information that aids in the later selection of events for individual analyses: the entire masking history is stored on disk along with the event record. In fact, the third-level masks exist solely to

allow rapid selection of relatively pure samples with which to begin analyses of events in various categories. These masks summarize the information obtained from all parts of the detector, and are described in Table B–3. Only events that are to be stored in these semi-permanent disk files undergo the additional analysis required to supply the information required by these masks.

Table B–1: First-level masks

Mask	Attribute number and description	Requirement
111	3 Central plus endcap shower chamber energy (in GeV)	≥ 5.7
	5 Number of inner drift tracks found in fast analysis	< 10
	7 1 if two central showers are back-to-back, 2 if back-to-back endcap showers	≥ 1
	16 Number of inner drift hits	< 600
112	3 Central plus endcap shower chamber energy (in GeV)	≥ 5.7
	4 Number of inner drift tracks found in fast analysis	≥ 1
	5 Number of inner drift tracks found in fast analysis	< 10
	6 1 if two fast inner drift tracks are back-to-back	$= 1$
	16 Number of inner drift hits	< 600
113	3 Central plus endcap shower chamber energy (in GeV)	≥ 5.7
	4 Number of inner drift tracks found in fast analysis	≥ 1
	5 Number of inner drift tracks found in fast analysis	< 10
	8 Number of trigger counters with time-of-flight information	≥ 1
	10 Number of sextants plus endcaps with shower energy more than .85 GeV	≥ 1
	13 1 if any back-to-back scintillators fired	$= 1$
	16 Number of inner drift hits	< 600
114	11 1 if event passes VAX software Bhabha filters 10 or 11	$= 1$
	16 Number of inner drift hits	< 600
115	3 Central plus endcap shower chamber energy (in GeV)	≥ 1.0
	4 Number of inner drift tracks found in fast analysis	≥ 1
	5 Number of inner drift tracks found in fast analysis	< 5
	6 1 if two fast inner drift tracks are back-to-back	$= 1$
	16 Number of inner drift hits	< 600
121	2 Central plus endcap hadron calorimeter energy (in GeV)	≥ 1.3
	4 Number of inner drift tracks found in fast analysis	≥ 1
	5 Number of inner drift tracks found in fast analysis	< 10
	8 Number of trigger counters with time-of-flight information	≥ 1
	13 1 if any back-to-back scintillators fired	$= 1$
	16 Number of inner drift hits	< 600

Table B–1 (cont.)

Mask	Attribute number and description		Requirement
131	3	Central plus endcap shower chamber energy (in GeV)	≥ 8.6
	5	Number of inner drift tracks found in fast analysis	< 3
	10	Number of sextants plus endcaps with shower energy more than .85 GeV	≥ 3
	14	Number of sextants plus endcaps with shower energy more than 2.9 GeV	≥ 2
	16	Number of inner drift hits	< 600
	17	Total energy (in multiples of beam energy)	< 3.0
141	16	Number of inner drift hits	< 600
	17	Total energy (in multiples of beam energy)	< 3.0
	18	Total energy (in multiples of beam energy)	≥ 1.0
151	4	Number of inner drift tracks found in fast analysis	≥ 2
	5	Number of inner drift tracks found in fast analysis	< 8
	16	Number of inner drift hits	< 100
	17	Total energy (in multiples of beam energy)	< 3.5
	18	Total energy (in multiples of beam energy)	$\geq .2$
	19	1 if full inner drift reconstruction has made a vertex-constrained fit	$= 1$
152	3	Central plus endcap shower chamber energy (in GeV)	≥ 2.9
	4	Number of inner drift tracks found in fast analysis	≥ 2
	5	Number of inner drift tracks found in fast analysis	< 8
	16	Number of inner drift hits	< 100
	19	1 if full inner drift reconstruction has made a vertex-constrained fit	$= 1$
153	2	Central plus endcap hadron calorimeter energy (in GeV)	≥ 2.0
	4	Number of inner drift tracks found in fast analysis	≥ 2
	5	Number of inner drift tracks found in fast analysis	< 8
	16	Number of inner drift hits	< 100
	19	1 if full inner drift reconstruction has made a vertex-constrained fit	$= 1$
154	5	Number of inner drift tracks found in fast analysis	< 6
	14	Number of sextants plus endcaps with shower energy more than 2.9 GeV	≥ 2
	16	Number of inner drift hits	< 600
	19	1 if full inner drift reconstruction has made a vertex-constrained fit	$= 1$

Table B–1 (cont.)

Mask	Attribute number and description	Requirement
161	2 Central plus endcap hadron calorimeter energy (in GeV)	$\geq .36$
	3 Central plus endcap shower chamber energy (in GeV)	≥ 1.4
	5 Number of inner drift tracks found in fast analysis	≥ 2
	8 Number of trigger counters with time-of-flight information	≥ 2
	10 Number of sextants plus endcaps with shower energy more than .85 GeV	≥ 2
	12 Number of sextants plus endcaps with shower energy more than .85 GeV, plus half number of trigger counters with time-of-flight information, plus number of sextants plus endcaps with hadronic energy at least 7.1 GeV	≥ 4
	16 Number of inner drift hits	< 600
162	2 Central plus endcap hadron calorimeter energy (in GeV)	$\geq .36$
	3 Central plus endcap shower chamber energy (in GeV)	≥ 1.4
	5 Number of inner drift tracks found in fast analysis	≥ 2
	8 Number of trigger counters with time-of-flight information	≥ 4
	9 Number of sextants with trigger counters fired	≥ 2
	10 Number of sextants plus endcaps with shower energy more than .85 GeV	≥ 1
	16 Number of inner drift hits	< 600
163	2 Central plus endcap hadron calorimeter energy (in GeV)	≥ 2.0
	3 Central plus endcap shower chamber energy (in GeV)	≥ 5.7
	5 Number of inner drift tracks found in fast analysis	≥ 2
	8 Number of trigger counters with time-of-flight information	≥ 3
	16 Number of inner drift hits	< 600
164	5 Number of inner drift tracks found in fast analysis	≥ 6
	14 Number of sextants plus endcaps with shower energy more than 2.9 GeV	≥ 2
	16 Number of inner drift hits	< 600
171	15 Flag for a possible neutral hadronic event	$= 1$
	16 Number of inner drift hits	< 10

Table B–2: Second-level masks[a]

Mask	Attribute number and description		Requirement
311	3	Central plus endcap shower chamber energy (in GeV)	≥ 5.7
	5	Number of tracks found in fast inner drift analysis	< 8
	15	Flag set if full inner drift analysis has found a good vertex, equal to the number of good inner drift tracks found.	≥ 2
	17	Total momentum of all inner drift tracks (GeV/c)	≥ 2.0
312	3	Central plus endcap shower chamber energy (in GeV)	≥ 8.6
	5	Number of tracks found in fast inner drift analysis	< 2
	7	1 if two central showers are back-to-back, 2 if back-to-back endcap showers	≥ 1
	16	Number of good tracks found in full inner drift analysis	< 1
313	3	Central plus endcap shower chamber energy (in GeV)	≥ 5.7
	5	Number of tracks found in fast inner drift analysis	< 8
	15	Flag set if full inner drift analysis has found a good vertex, equal to the number of good inner drift tracks found.	≥ 2
	16	Number of good tracks found in full inner drift analysis	< 3
	17	Total momentum of all inner drift tracks (GeV/c)	≥ 2.0
	18	Minimum angle (°) between any inner drift track and beam axis	≥ 55
314	3	Central plus endcap shower chamber energy (in GeV)	≥ 5.7
	5	Number of tracks found in fast inner drift analysis	< 8
	16	Number of good tracks found in full inner drift analysis	< 2
	17	Total momentum of all inner drift tracks (GeV/c)	≥ 2.0
	18	Minimum angle (°) between any inner drift track and beam axis	≥ 20
321	2	Central plus endcap hadron calorimeter energy (in GeV)	≥ 1.3
	5	Number of tracks found in fast inner drift analysis	< 8
	15	Flag set if full inner drift analysis has found a good vertex, equal to the number of good inner drift tracks found.	≥ 2
	17	Total momentum of all inner drift tracks (GeV/c)	≥ 2.0

Table B–2 (cont.)

Mask	Attribute number and description	Requirement
331	2 Central plus endcap hadron calorimeter energy (in GeV)	≥ 1.3
	5 Number of tracks found in fast inner drift analysis	< 8
	15 Flag set if full inner drift analysis has found a good vertex, equal to the number of good inner drift tracks found.	≥ 2
	16 Number of good tracks found in full inner drift analysis	< 4
	17 Total momentum of all inner drift tracks (GeV/c)	≥ 2.0
	19 Acollinearity (°) between two inner drift tracks with maximum momenta	≥ 10
332	3 Central plus endcap shower chamber energy (in GeV)	≥ 5.7
	5 Number of tracks found in fast inner drift analysis	< 8
	15 Flag set if full inner drift analysis has found a good vertex, equal to the number of good inner drift tracks found.	≥ 2
	16 Number of good tracks found in full inner drift analysis	< 4
	17 Total momentum of all inner drift tracks (GeV/c)	≥ 2.0
	19 Acollinearity (°) between two inner drift tracks with maximum momenta	≥ 10
333	2 Central plus endcap hadron calorimeter energy (in GeV)	≥ 1.3
	3 Central plus endcap shower chamber energy (in GeV)	≥ 4.3
	5 Number of tracks found in fast inner drift analysis	< 8
	15 Flag set if full inner drift analysis has found a good vertex, equal to the number of good inner drift tracks found.	≥ 2
	16 Number of good tracks found in full inner drift analysis	< 4
	17 Total momentum of all inner drift tracks (GeV/c)	≥ 2.0
	19 Acollinearity (°) between two inner drift tracks with maximum momenta	≥ 20

Table B–2 (cont.)

Mask	Attribute number and description	Requirement
334	3 Central plus endcap shower chamber energy (in GeV)	≥ 5.7
	5 Number of tracks found in fast inner drift analysis	< 8
	15 Flag set if full inner drift analysis has found a good vertex, equal to the number of good inner drift tracks found.	≥ 2
	16 Number of good tracks found in full inner drift analysis	< 4
	17 Total momentum of all inner drift tracks (GeV/c)	≥ 2.0
	19 Acollinearity (°) between two inner drift tracks with maximum momenta	≥ 20
335	2 Central plus endcap hadron calorimeter energy (in GeV)	≥ 1.6
	3 Central plus endcap shower chamber energy (in GeV)	≥ 2.1
	10 Number of tracks found in central plus endcap hadron calorimeter	≥ 1
	15 Flag set if full inner drift analysis has found a good vertex, equal to the number of good inner drift tracks found.	≥ 2
	16 Number of good tracks found in full inner drift analysis	< 3
	17 Total momentum of all inner drift tracks (GeV/c)	≥ 3.5
	19 Acollinearity (°) between two inner drift tracks with maximum momenta	≥ 10
341	4 Total energy (in multiples of beam energy)	≥ 1.0
	6 Total energy (in multiples of beam energy)	< 3.5
	15 Flag set if full inner drift analysis has found a good vertex, equal to the number of good inner drift tracks found.	≥ 2
	17 Total momentum of all inner drift tracks (GeV/c)	≥ 2.0

Table B–2 (cont.)

Mask	Attribute number and description	Requirement
342	3 Central plus endcap shower chamber energy (in GeV)	≥ 8.6
	5 Number of tracks found in fast inner drift analysis	< 3
	6 Total energy (in multiples of beam energy)	< 3.0
	9 Number of sextants plus endcaps with shower energy more than .85 GeV	≥ 3
	12 Number of sextants plus endcaps with shower energy more than 2.9 GeV	≥ 2
	13 Imbalance (0 if energy uniformly distributed, near 1 if lopsided)	$< .5$
	16 Number of good tracks found in full inner drift analysis	< 1
343	4 Total energy (in multiples of beam energy)	$\geq .2$
	6 Total energy (in multiples of beam energy)	< 3.5
	10 Number of tracks found in central plus endcap hadron calorimeter	≥ 1
	15 Flag set if full inner drift analysis has found a good vertex, equal to the number of good inner drift tracks found.	≥ 2
	17 Total momentum of all inner drift tracks (GeV/c)	≥ 2.0
344	15 Flag set if full inner drift analysis has found a good vertex, equal to the number of good inner drift tracks found.	≥ 3
	17 Total momentum of all inner drift tracks (GeV/c)	≥ 2.0
345	14 Flag for possible neutral hadronic event	≥ 1
	16 Number of good tracks found in full inner drift analysis	< 1
351	2 Central plus endcap hadron calorimeter energy (in GeV)	≥ 1.3
	3 Central plus endcap shower chamber energy (in GeV)	≥ 5.7
	5 Number of tracks found in fast inner drift analysis	< 8
	15 Flag set if full inner drift analysis has found a good vertex, equal to the number of good inner drift tracks found.	≥ 2
	17 Total momentum of all inner drift tracks (GeV/c)	≥ 2.0

Table B–2 (cont.)

Mask	Attribute number and description	Requirement
352	2 Central plus endcap hadron calorimeter energy (in GeV)	≥ 1.0
	3 Central plus endcap shower chamber energy (in GeV)	≥ 2.9
	5 Number of tracks found in fast inner drift analysis	< 8
	15 Flag set if full inner drift analysis has found a good vertex, equal to the number of good inner drift tracks found.	≥ 2
	17 Total momentum of all inner drift tracks (GeV/c)	≥ 2.0
353	2 Central plus endcap hadron calorimeter energy (in GeV)	≥ 1.8
	5 Number of tracks found in fast inner drift analysis	< 8
	15 Flag set if full inner drift analysis has found a good vertex, equal to the number of good inner drift tracks found.	≥ 2
	17 Total momentum of all inner drift tracks (GeV/c)	≥ 2.0
354	2 Central plus endcap hadron calorimeter energy (in GeV)	≥ 1.0
	3 Central plus endcap shower chamber energy (in GeV)	≥ 1.0
	5 Number of tracks found in fast inner drift analysis	< 8
	15 Flag set if full inner drift analysis has found a good vertex, equal to the number of good inner drift tracks found.	≥ 2
	17 Total momentum of all inner drift tracks (GeV/c)	≥ 2.0
361	2 Central plus endcap hadron calorimeter energy (in GeV)	≥ 2.0
	3 Central plus endcap shower chamber energy (in GeV)	≥ 5.7
	8 Number of trigger counters with time-of-flight information	≥ 1
	11 Number of sextants plus endcaps with shower energy more than .85 GeV, plus half number of trigger counters with time-of-flight information, plus number of sextants plus endcaps with hadronic energy at least 7.1 GeV	≥ 4
	15 Flag set if full inner drift analysis has found a good vertex, equal to the number of good inner drift tracks found.	≥ 2
	17 Total momentum of all inner drift tracks (GeV/c)	≥ 2.0

Table B–2 (cont.)

Mask	Attribute number and description	Requirement
362	3 Central plus endcap shower chamber energy (in GeV)	≥ 5.7
	8 Number of trigger counters with time-of-flight information	≥ 1
	12 Number of sextants plus endcaps with shower energy more than 2.9 GeV	≥ 2
	15 Flag set if full inner drift analysis has found a good vertex, equal to the number of good inner drift tracks found.	≥ 3
	17 Total momentum of all inner drift tracks (GeV/c)	≥ 2.0
363	2 Central plus endcap hadron calorimeter energy (in GeV)	≥ 2.0
	3 Central plus endcap shower chamber energy (in GeV)	≥ 5.7
	8 Number of trigger counters with time-of-flight information	≥ 3
	15 Flag set if full inner drift analysis has found a good vertex, equal to the number of good inner drift tracks found.	≥ 2
	17 Total momentum of all inner drift tracks (GeV/c)	≥ 2.0
364	2 Central plus endcap hadron calorimeter energy (in GeV)	≥ 2.0
	3 Central plus endcap shower chamber energy (in GeV)	≥ 2.9
	8 Number of trigger counters with time-of-flight information	≥ 2
	15 Flag set if full inner drift analysis has found a good vertex, equal to the number of good inner drift tracks found.	≥ 2
	17 Total momentum of all inner drift tracks (GeV/c)	≥ 2.0

Table B–2 (cont.)

Mask	Attribute number and description	Requirement
371	2 Central plus endcap hadron calorimeter energy (in GeV)	≥ 8.9
	4 Total energy (in multiples of beam energy)	$\geq .8$
	6 Total energy (in multiples of beam energy)	< 3.5
	13 Imbalance (0 if energy uniformly distributed, near 1 if lopsided)	$< .4$
	15 Flag set if full inner drift analysis has found a good vertex, equal to the number of good inner drift tracks found.	≥ 3
	17 Total momentum of all inner drift tracks (GeV/c)	≥ 2.0
372	2 Central plus endcap hadron calorimeter energy (in GeV)	≥ 4.3
	4 Total energy (in multiples of beam energy)	$\geq .8$
	6 Total energy (in multiples of beam energy)	< 3.5
	13 Imbalance (0 if energy uniformly distributed, near 1 if lopsided)	$< .5$
	15 Flag set if full inner drift analysis has found a good vertex, equal to the number of good inner drift tracks found.	≥ 4
	17 Total momentum of all inner drift tracks (GeV/c)	≥ 2.0
373	4 Total energy (in multiples of beam energy)	$\geq .8$
	6 Total energy (in multiples of beam energy)	< 3.5
	13 Imbalance (0 if energy uniformly distributed, near 1 if lopsided)	$< .6$
	15 Flag set if full inner drift analysis has found a good vertex, equal to the number of good inner drift tracks found.	≥ 5
	17 Total momentum of all inner drift tracks (GeV/c)	≥ 2.0

[a]A 'good inner drift track' is one that verticizes and has either six or more hits or 5 hits and momentum greater than 1 GeV/c. A 'good inner drift vertex' is a primary vertex that satisfies the criteria for a vertex-constrained fit, is located within a reasonable volume from the interaction point, and is the origin of at least one good track with an angle of at least 17° from the beam pipe.

Table B–3: Third-level masks[a]

Mask	Meaning
411	Exactly two extended shower sextants have energy greater than 1.5 GeV, and these are back-to-back
412	Acollinearity of two inner drift tracks with maximum momenta is $< 10°$
413	Net charge of good inner drift tracks is zero
414	Two showers with maximum energy are back-to-back (within 3° in ϕ if in central section, 5° of collinear if in endcap)
415	Exactly three extended shower sextants have energy greater than 1.5 GeV, and these are not all on one side of the detector
416	Total shower energy is greater than beam energy
417	Total shower energy is $< 3E_{beam}$
418	Acollinearity of two inner drift tracks with maximum momenta is $< 2.5°$
419	$< 5.0°$
42n	At least n good inner drift tracks found ($0<n<7$)
431	Total energy of event greater than: 1/3 beam energy
432	2/3 beam energy
433	beam energy
434	two times beam energy
435	three times beam energy
436	four times beam energy
441	θ of energy thrust axis is greater than: 15°
442	30°
443	55°
444	At least one track found in outer drift reconstruction
445	Energy imbalance (sum of north/south, top/bottom, and left/right asymmetry) $< .4$
446	Energy imbalance $< .6$
451	Total momentum of all inner drift tracks is greater than 3 GeV/c
461	Global track fitting routine has found: at least one electron
462	at least two electrons
463	at least one muon
464	at least two muons
465	at least one pion
466	at least one neutral
467	at least one rho
47n	Minimum number of good inner drift tracks in a hemisphere is $< n$ $(0 < n < 6)$

Table B–3 (cont.)

Mask	Meaning	
511	Momentum thrust axis is more than 4° in ϕ from the edge of a sextant.	
512	All good inner drift tracks are between 20° and 25° from beam pipe	
513	All good inner drift tracks have ϕ more than 5° from the edge of a twelfth	
531	Maximum inner drift track momentum is greater than 2.5 GeV/c	
541	θ of momentum thrust axis is greater than:	15°
542		30°
543		55°
61n	Number of inner drift tracks = n (or $\geq n$, for $n = 9$)	
62n	Number of good inner drift tracks associated with the primary vertex = n (or $\geq n$, for $n = 9$)	

[a]A 'good inner drift track' is one that verticizes and has either six or more hits or 5 hits and momentum greater than 1 GeV/c. An 'extended shower sextant' is a shower chamber sextant plus the two twelfths from each endcap that cover the same range of ϕ. A 'hemisphere' is either side of a plane perpendicular to the energy thrust axis.

Bibliography

Abramowicz, H., *et al.*, Z. Phys. **C15**, 19 (1982).

Abrams, G. S. *et al.*, Phys. Rev. Lett. **33**, 1453 (1974).

Adler, S. L., *Lectures on Elementary Particles and Quantum Field Theory*, edited by S. Deser *et al.*, (MIT, Cambridge, 1970).

Ali, A., E. Pietarinen, and J. Willrodt, DESY Report No. DESY T-80/01, 1980.

Althoff, M., *et al.*, DESY Report No. DESY 83/10, 1983.

Andrews, D., *et al.*, Cornell Report No. CLNS 82/547.

Appelquist, T., R. M. Barnett, and K. Lane, "Charm and Beyond," in *Annual Review of Nuclear and Particle Science*, edited by J. D. Jackson *et al*, (Annual Reviews, Palo Alto, 1978).

Atwood, W. B., *et al.*, SLAC Report No. SLAC-PUB-2981, 1982.

Aubert, J., *et al.*, Phys. Rev. Lett. **33**, 1404 (1974).

Augustin, J.-E., *et al.*, Phys. Rev. Lett. **33**, 1406 (1974).

Bacino, W., *et al.*, Phys. Rev. Lett. **40**, 671 (1978).

Basham, C. L., L. S. Brown, S. D. Ellis, and S. T. Love, Phys. Rev. **D17** 2298, (1978); Phys. Rev. Lett. 41 1585, (1978); and Phys. Rev. **D19** 2018,

(1979).

Bebek, C., *et al.*, Phys. Rev. Lett. **49**, 610 (1982).

Bjorken, J. D., Phys. Rev. **179**, 1547 (1969).

Bjorken, J. D., Phys. Rev. **D17**, 171 (1978).

Breidenbach, M., E. Frank, Jim Hall, D. Nelson, *Semi-Autonomous Controller for Data Acquisition: The Brilliant ADC,* SLAC Report SLAC-PUB-2032, 1977.

Brodsky, S. J., C. Peterson, and N. Sakai, Phys. Rev. **D23**, 2745 (1981).

Chadwick, K., *et al.*, Phys. Rev. **D27**, 475 (1983).

Ellis, J. "Phenomenology of Unified Gauge Theories," LAPP Report No. LAPP-TH-48 (1981).

Ellis, J. "Weak Interactions at High Energies," in *Procedings of the Summer Institute on Particle Physics*, edited by M. Zipf, (SLAC, Stanford, 1978).

Ellis, J. and M. K. Gaillard, "Theoretical Remarks," in CERN Report No. CERN 76-18 (1976).

Farhi, E., Phys. Rev. Lett. **39**, 1587 (1977).

Fernandez, E. *et al.*, Phys. Rev. Lett. **50**, 1238 (1983).

Feynman, R. P., Phys. Rev. Lett. **23**, 1415 (1969) and *Photon-Hadron Interactions*, (Benjamin, New York, 1972).

Field, R. D., and R. P. Feynman, Nucl. Phys. **B136**, 1 (1977) and Phys. Rev. **D15**, 2590 (1977).

Fritzsch, H., M. Gell-Mann, and H. Leutweyler, Phys. Lett. **B47** 365, (1973).

Gell-Mann, M., Phys. Lett. **8**, 214 (1964).

Georgi, H., S. L. Glashow, Nucl. Phys. **B159**, 29 (1979).

Glashow, S. L., J. Iliopoulos, and L. Maiani, Phys. Rev. **D2**, 1285 (1970).

Glashow, S. L., Nucl. Phys. **22**, 579 (1961).

Green, J., *et al.*, Cornell Report No. CLNS 82/547.

Greenberg, O. W., Phys. Rev. Lett. **13**, 598 (1964).

Gross, D. J., and F. Wilczek, Phys. Rev. Lett. **30**, 1343 (1973) and Phys. Rev. **D8**, 3633 (1973).

Gross, D. J., and R. Jackiw, Phys. Rev. **D6**, 477 (1972).

Hagelin, J. S., Nucl. Phys. **B193**, 123 (1981).

Han, M. Y., and Y. Nambu, Phys. Rev. **B139**, 1006 (1965).

Herb, S. W., *et al.*, Phys. Rev. Lett. **39**, 252 (1977).

Kane, G. L., and M. E. Peskin, Nucl. Phys. **B195**, 29 (1982).

Kim, J. J., P. Longacker, M. Levine, and H. H. Williams, Rev. Mod. Phys. **53**, 211 (1981).

Kleinknecht, K., and B. Renk, University of Dortmund Report No. UNIDO-82/274, 1982.

Kobayashi, M., and K. Maskawa, Progr. Theor. Phys. **49**, 652 (1973).

Lee, T. D., *Particle Physics and Introduction to Field Theory*, (Harwood, New York, 1981).

Mess, K. H., and B. H. Wiik, DESY Report No. DESY 82-011 (1982).

Nelson, M. E., *et al.*, Phys. Rev. Lett. **50**, 1542 (1983).

Perl, M. L., *et al.*, Phys. Rev. Lett. **35**, 1489 (1975).

Peterson, C., D. Schlatter, I. Schmitt, and P. M. Zerwas, Phys. Rev. **D27**, 105 (1983).

Politzer, H. D., Phys. Rev. Lett. **30**, 1346 (1973).

Ritson, D. M., SLAC Report No. SLAC-PUB-2986, 1982.

Salam, A., *Elementary Particle Physics: Relativistic Groups and Analyticity*, edited by N. Svartholm, (Almquist & Wiksell, Stockholm, 1968), p. 367.

Schindler, R. H., *et al.*, Phys. Rev. **D24**, 78 (1981).

Schlatter, D., SLAC Report No. SLAC-PUB-2982 (1978).

Soding, P. and G. Wolf, "Experimental Evidence on QCD," in *Annual Review of Nuclear and Particle Science*, edited by J. D. Jackson *et al*, (Annual Reviews, Palo Alto, 1981).

Suzuki, M., Phys. Lett. **71B**, 139 (1977).

Ushida, N., *et al.*, Phys. Lett. **121B**, 292 (1983).

Weinberg, S., Phys. Rev. Lett. **19**, 1264 (1967).

Wilczek, F., "Quantum Chromodynamics," in *Annual Review of Nuclear and Particle Science*, edited by J. D. Jackson *et al*, (Annual Reviews, Palo Alto, 1982).

Yelton, J. M., *et al.*, Phys. Rev. Lett. **49**, 430 (1982).

Zweig, G., CERN Report No. TH 401:412 (1964).